Half-metallicity versus symmetry in half-Heusler alloys based on Pt, Ni, and Co: An *ab initio* study

Madhusmita Baral[1,2] and Aparna Chakrabarti[2,3]

[1]*Synchrotrons Utilization Section, Raja Ramanna Centre for Advanced Technology, Indore 452013, India*

[2]*Homi Bhabha National Institute, Training School Complex, Anushakti Nagar, Mumbai 400094, India*

[3]*Theory and Simulations Laboratory, HRDS, Raja Ramanna Centre for Advanced Technology, Indore 452013, India*

(Received 2 May 2017; revised manuscript received 10 January 2019; published 21 May 2019)

Using first-principles calculations based on density functional theory, we study the geometric, electronic, and magnetic properties of Pt-, Ni-, and Co-based half-Heusler alloys, namely, Pt*BC*, Ni*BC*, and Co*BC* (B = Cr, Mn, and Fe; C = Al, Si, P, S, Ga, Ge, As, Se, In, Sn, Sb, and Te). We calculate the formation energy of these alloys in various crystal symmetries, which include the cubic $C1_b$ ($F\bar{4}3$m), orthorhombic (*Pnma*), as well as hexagonal ($P\tilde{6}2m$ and $P6_3/mmc$) structures. It has been observed that, out of the alloys studied, only 18 are energetically stable in the cubic lowest energy structure. These alloys primarily have either a C atom or an A atom (Pt, Ni, or Co) with a high atomic number. We also observe that, along with the alloys with C atoms from groups IIIA, IVA, and VA, alloys with C atoms from group VIA are also found to be, by and large, energetically stable. Furthermore, among the energetically stable cubic alloys, only CoMnSb, CoMnTe, and NiMnSb show the half-metallic property. Under volume-conserving tetragonal distortion, the half-metallic property is completely destroyed in CoMnSb, whereas CoMnTe and NiMnSb maintain half-metallicity for a c/a value from 0.8 to 1.2 for CoMnTe and from 1.0 to 1.2 for NiMnSb, respectively. From the theoretical calculations, many of the half-Heusler alloys are reported to be half-metals in the cubic phase, but these are synthesized in noncubic structures. We analyze the magnetic moment, the electronic density of states, and the spin polarization at the Fermi level, in detail, to find whether a material in the noncubic lowest energy structure exhibits half-metallicity or not. Based on these analyses, the possibility of existence of any one-to-one relationship between the cubic symmetry and the half-metallicity in these half-Heusler alloys is explored. We predict about the existence of a new noncubic half-Heusler alloy with a substantially low density of states at one of the spin channels and subsequently a reasonably high spin polarization at the Fermi level. However, it is found that for alloys in the lowest energy structure, cubic symmetry is necessary for 100% spin polarization. Furthermore, for Pt-based alloys, the effects of spin-orbit coupling (SOC) have been explored. It is observed that inclusion of SOC in the Pt-based alloys does not play a crucial role in either the geometric or the electronic structure consideration.

DOI: 10.1103/PhysRevB.99.205136

I. INTRODUCTION

The prediction and development of new half-metals are of immense interest due to their potential for technological applications [1,2]. The half-metals are a type of materials where spin polarization (SP) at the Fermi level (E_F) is 100%. Ever since half-metallicity was predicted in the half-Heusler alloys (HHAs) NiMnSb and its isoelectronic alloy PtMnSb, on the basis of band-structure calculations [3], the field of half-metallic HHAs has attracted the interest of researchers.

A large amount of theoretical and experimental work on NiMnSb, PtMnSb, and substitution at their different atomic sites has been reported in the literature, and in most of the alloys, Curie temperature (T_C) is observed to be above room temperature, which is essential for their application as an efficient and useful spin-injector material [4–19]. In order to strengthen the search for new half-metals, a large number of *ABC*- and A_2BC-type Heusler alloys have been theoretically studied in the literature, where A and B are transition-metal atoms and C is an *sp* element [20–39]. Although most of the studied HHAs show the half-metallic property in the cubic $C1_b$ phase with $F\bar{4}3m$ space group, only a few of these have been experimentally synthesized in the cubic phase [6,8–19]. On the contrary, many of the HHA samples have been experimentally synthesized in noncubic symmetries but there is no explicit discussion on the magnetic and half-metallic properties of these materials in the literature [40–60].

In this work, we address four points:

(1) In the literature, although quite a few Co*BC*, Ni*BC*, and Pt*BC* HHAs are theoretically predicted to be half-metallic in cubic $C1_b$ structure, many of these are experimentally synthesized in one noncubic phase or other. Since there are only a few reports on the structural stability of these systems, we study in detail the structural stability versus symmetry of, in total, 108 Co-, Ni-, and Pt-based HHAs in this work. For this purpose, we analyze formation energy (E_{form}) in different possible symmetries to find the lowest energy structure (LES) for each of these materials. From our study, we find that only 18 alloys have the lowest E_{form} in the cubic $C1_b$ phase and the rest of the alloys have noncubic LES. Furthermore, we try to understand the trend in similarities and differences in the magnetic and electronic properties of these materials in cubic and noncubic phases.

(2) In the literature, Pt*BC* HHAs have been much less studied in comparison to Ni- and Co-based alloys. Therefore, in this work, we study in detail the structural, magnetic, and

electronic properties of Pt-based alloys. Furthermore, we have also studied the effect of spin-orbit coupling (SOC) on the magnetic and electronic properties of Pt*BC* HHAs, as Pt is one of the high-*Z* elements.

(3) As discussed above, many of the *ABC*-type HHAs are experimentally synthesized in noncubic symmetries although these are theoretically predicted to show the half-metallic property in the cubic phase. Here in this work, we want to probe the possibility of existence of any half-metallic-like property in these alloys in their experimental ground state structure (GSS) or the LES by analyzing the electronic structure. Additionally, we wish to explore if there is any *one-to-one relationship* between the *cubic symmetry* and the *half-metallicity* in the alloys studied in this work.

(4) Furthermore, we want to explore the possibility of existence of any new and novel noncubic half-metallic-like HHA. Subsequently, we predict the possibility of a new HHA exhibiting high SP at the E_F in noncubic symmetry.

In the next section, we discuss the methods of calculations, which are based on density functional theory (DFT). In the section following the methodology, we present our results and discussion on the same. Finally, we summarize and conclude in the last section.

II. METHOD

First, we discuss in detail the space groups we have considered in our present work. We probe four different crystal symmetries, which have been reported for various HHAs so far, namely, cubic $C1_b$ (space group $F\bar{4}3m$, no. 216), orthorhombic (space group *Pnma*, no. 62), as well as hexagonal structures (space groups $P\bar{6}2m$, no. 189, and $P6_3/mmc$, no. 194). We have not carried out calculations on any disordered structure due to the lack of any systematic input of structural data for these materials. In this paper, we have carried out calculations on Co-, Ni-, and Pt-based systems; Co, Ni, and Pt are taken as the *A* atom. Cr, Mn, and Fe have been considered as the *B* atom since we are interested in magnetic alloys and these *B* atoms are known to have high atomic moments. Furthermore, for the *C* atom, we have taken the following elements: Al, Si, P, S, Ga, Ge, As, Se, In, Sn, Sb, and Te. In total, we have studied 108 different HHAs.

In the LES, the most well-studied HHA NiMnSb has a $C1_b$ structure with space group $F\bar{4}3m$, that consists of four interpenetrating face-centered-cubic (fcc) lattices with fractional coordinates, (0.25, 0.25, 0.25), (0.75, 0.75, 0.75), (0.5, 0.5, 0.5), and (0.0, 0.0, 0.0). We label these sublattices as W, X, Y, and Z, respectively. In the $C1_b$ structure of NiMnSb, the Ni atoms occupy the W sublattice and the X sublattice remains empty. Furthermore, Mn and Sb atoms occupy the Y and Z sublattices, respectively.

CoMnGe is a HHA which exhibits an orthorhombic structure with *Pnma* space group. All the atoms here occupy sites with a Wyckoff position of 4c. The symmetry equivalent fractional coordinates according to the 4c point-group symmetry are as follows: $(x, 0.25, z)$, $(-x+0.5, 0.75, z+0.5)$, $(-x, 0.75, -z)$, $(x+0.5, 0.25, -z+0.5)$, where x and z are different for different atoms.

NiMnGa assumes a hexagonal structure ($P6_3/mmc$ space group). The Ni atom occupies a site with a point-group symmetry of 2d,(1/3, 2/3, 3/4) and (2/3, 1/3 and 1/4); the Mn atom occupies site with 2a symmetry, (0,0,0) and (0,0,0.5); and the Ga atom is found at the site with 2c symmetry, (1/3,2/3,1/4) and (2/3,1/3,3/4).

NiFeAs is found in a hexagonal structure ($P\bar{6}2m$ space group). The Ni atom occupies the site with 3f point-group symmetry $(x, 0, 0)$, $(0, x, 0)$, $(-x, -x, 0)$; the Fe atom has the preference for a site which has a 3g point-group symmetry with fractional coordinates as follows: $(x, 0, 0.5)$, $(0, x, 0.5)$, $(-x, -x, 0.5)$. The As atom occupies two different Wyckoff positions with 1b and 2c point-group symmetries with fractional coordinates, (0,0,0) and (1/3,2/3,0.5) and (2/3,1/3,0.5), respectively.

The equilibrium lattice constants and fractional coordinates of all these alloys have been optimized by doing full geometry optimization using the Vienna Ab initio Simulation Package (VASP) [61–63], which has been used in combination with the projector augmented wave (PAW) method [64]. We have interchanged the Wyckoff positions of the *A* and *B* atoms in the case of $P6_3/mmc$ and $P\bar{6}2m$ space groups as well as varied the variable fractional coordinates, x_A and x_B, in the case of the latter space group to find the structure with the lowest E_{form}. x and z have been varied for all three atoms A, B, and C in the case of the *Pnma* space group to arrive at the structure which yields the lowest E_{form} among them all.

For the exchange-correlation functional, the generalized gradient approximation (GGA) over the local density approximation (LDA) has been used [65]. We use an optimum energy cutoff of 500 eV for the plane-wave basis set. The final energies have been calculated with a k mesh for which the convergence has been tested. The energy and the force tolerance for our calculations were 10 μeV and 10 meV/Å, respectively. The mixing or formation energies (E_{form}) have been calculated [63] for probing the energetic stability of a material, using the equation $E_{\text{form}} = E_{\text{tot}} - \Sigma_i c_i E_i$, where i denotes different types of atoms present in the unit cell of the material with concentration c_i and E_i is the standard state (bulk) energy of the corresponding atom, i [63]. These energies were then analyzed to establish the energetic stability of the alloys in different crystal symmetries. The optimized geometries of the systems are compared with the results obtained in the literature, wherever the results are available. The detailed converged structures (fractional coordinates and lattice constants) are reported in the Supplemental Material [66]. For the Pt-based alloys, the full geometry optimization was carried out, without and with SOC, using the VASP package.

For in-depth understanding of the magnetic and electronic properties, we have carried out relativistic spin-polarized *all-electron* calculations for the optimized structures of all the systems. These calculations have been performed using the full potential linearized augmented plane-wave (FPLAPW) program with the GGA for the exchange-correlation functional [65,67]. For obtaining the electronic properties, the Brillouin-zone (BZ) integration was carried out using the tetrahedron method with Blöchl corrections [67]. An energy cutoff for the plane-wave expansion of about 14 Ry is typically used. The cutoff for charge density is $G_{\max} = 14$. The numbers of k points for the self-consistent field cycles in the irreducible BZ are about 300, 600, and 2300 in the cases of cubic, hexagonal, and orthorhombic, respectively.

TABLE I. Number of valence electrons per formula unit (Z_v). Space group of the calculated LES of Co*BC* alloys: cubic ($F\bar{4}3m$), hexagonal ($P6_3/mmc$ and $P\bar{6}2m$), and orthorhombic ($Pnma$). μ_T and SP are the calculated total spin magnetic moment and spin polarization of the LES, respectively. The space group of the experimentally observed structure is shown along with the lattice parameter and total spin magnetic moment.

Calculation						Experiment		
Material	Z_v	Space group	Lattice parameter (a, b, c) (Å)	μ_T (μ_B)	SP	Space group	Lattice parameter (a, b, c) (Å)	μ_T (μ_B)
CoCrAl	18	***Pnma***	(4.90, 4.03, 7.34)	1.43	54.5			
CoMnAl	19	***Pnma***	(5.05, 3.99, 7.31)	3.32	18.4			
CoFeAl	20	***Pnma***	(4.96, 3.95, 7.30)	3.26	49.7			
CoCrGa	18	***Pnma***	(4.94, 4.05, 7.32)	1.57	52.4			
CoMnGa	19	***Pnma***	(5.7, 4.05, 7.24)	4.12	34.7			
CoFeGa	20	***Pnma***	(5.00, 3.96, 7.33)	3.41	45.3			
CoCrSi	19	***Pnma***	(5.75, 3.61, 6.73)	0.99	36.9	*Pnma* [47]	(5.77, 3.66, 6.78) [47]	
CoMnSi	20	***Pnma***	(5.72, 3.66, 6.87)	3.49	41.2	*Pnma* [44,47]	(5.84, 3.68, 6.84) [47]	
CoFeSi	21	***Pnma***	(5.60, 3.61, 6.79)	2.56	66.0	*Pnma* [47]	(4.94, 3.78, 7.17) [47]	
CoCrGe	19	***P6$_3$/mmc***	(4.10, 5.11)	2.40	7.03	$P6_3/mmc$ [48]	(4.09, 5.15) [48]	
CoMnGe	20	***Pnma***	(5.83, 3.78, 7.08)	3.75	44.0	*Pnma* [43]	(5.95, 3.82, 7.06) [43]	
						$P6_3/mmc$ [42,43,53,59]	(4.07, 5.28) [42]	2.5 [42]
CoFeGe	21	***Pnma***	(5.00, 3.92, 7.31)	2.72	63.7	$P6_3/mmc$ [9,42]	(4.00, 5.04) [9]	2.5 [9]
CoCrP	20	***Pnma***	(5.73, 3.52, 6.68)	1.93	76.3	*Pnma* [51,52]	(5.77, 3.55, 6.68) [51]	
CoMnP	21	***Pnma***	(5.89, 3.46, 6.68)	2.99	13.8	*Pnma* [50–52]	(5.95, 3.50, 6.73) [50]	3.05 [50]
CoFeP	22	***Pnma***	(5.69, 3.52, 6.52)	2.04	23.2	*Pnma* [50–52]	(5.75, 3.53, 6.60) [50]	1.9 [50]
CoCrAs	20	***Pnma***	(5.95, 3.71, 6.99)	2.18	52.2	$P\bar{6}2m$ [51,52]	(6.07, 3.66) [51]	
CoMnAs	21	***Pnma***	(6.31, 3.62, 6.97)	3.10	52.9	*Pnma* [51–53]	(6.21, 3.72, 7.01) [53]	2.89 [53]
CoFeAs	22	***Pnma***	(5.92, 3.67, 6.82)	2.14	45.9	$P\bar{6}2m$ [51,52]	(6.07, 3.58) [51]	
CoMnSb	21	***F$\bar{4}$3m***	(5.82)	3.00	100	$F\bar{4}3m$ [9,20]	(5.875) [9]	3.93 [9]
						$Fm\bar{3}m$ [18]	(11.73) [18]	3.93 [18]
CoFeSb	22	***F$\bar{4}$3m***	(5.81)	3.99	58.3			
CoCrS	21	***Pnma***	(5.92, 3.47, 6.73)	2.94	58.0			
CoMnS	22	***P$\bar{6}$2m***	(5.79, 3.5)	2.39	13.8			
CoFeS	23	***Pnma***	(5.84, 3.64, 6.44)	2.98	33.6			
CoMnSe	22	***F$\bar{4}$3m***	(5.63)	4.00	97.8			
CoMnTe	22	***F$\bar{4}$3m***	(5.86)	4.00	100			
CoFeTe	23	***F$\bar{4}$3m***	(5.86)	4.42	69.5			

The convergence criterion for the total energy E_{tot} is about 0.1 mRy per atom. The charge convergence is set to 0.0001.

III. RESULTS AND DISCUSSION

A. Structural stability of *ABC* half-Heusler alloys

Co*BC*, Ni*BC*, and Pt*BC* alloys, 36 each, have been studied in this work. Since it is important to probe first the structural stability of these alloys, in this sub-section we explore this by analyzing their E_{form} calculated for different crystal structures. We find that a total of 25 alloys possess positive E_{form} in any of the structures probed here, which suggests that synthesizing these materials may not be possible. Among the Co*BC* and Ni*BC* alloys, the ones with positive E_{form} generally contain a larger *C* atom (i.e., In, Sn, Se, and Te), whereas in case of Pt*BC*, the alloys with positive E_{form} possess a *C* atom mainly from group VIA.

1. Structural stability of Co*BC half-Heusler alloys*

The number of valence electrons per formula unit (Z_v), optimized lattice parameters, total spin magnetic moment, and SP for the LES of the Co*BC* alloys are presented in Table I along with the experimental structure (space group and lattice parameters) and total spin magnetic moment, wherever available. As can be seen from Table I, the lattice parameters for the LES match well with the GSS within an error bar of about 3%, except for only one case, i.e., CoFeSi, where the values of lattice parameters are slightly higher. This difference may have arisen because CoFeSi is experimentally found to be a mixture of two phases [47]. Our calculated total magnetic moment of the alloys, in general, is found to be slightly higher than the experimentally measured value. This may be due to the variation in composition or small impurity phase or structural disorder present in the actual sample. In our recent study on NiCrGa HHAs [68], we found that the presence of structural disorder significantly disturbed the magnetic property. Although there are many experimental reports available, not much work on the theoretical study of these alloys in noncubic structure is available in literature. However, for the CoMnGe alloy, there are some theoretical works present in the literature, where the calculated magnetic moment as well as the lattice parameters are in close agreement with our results [46,69,70].

From Table I, we observe that for the alloys with smaller *C* atoms, the LES mainly assumes either an orthorhombic or one of the hexagonal structures. The high-symmetry cubic half-Heusler structure is the LES for alloys with large *C* atoms (i.e., Se, Sb, and Te) and *B* atom being Mn or Fe. There is some correlation observed between the LES and the Z_v value. When Z_v is less than 20, the noncubic phase is the LES for the alloys with any *C* atom. On the other hand, when Z_v is greater than 20, the noncubic phase is the LES for the alloys with smaller *C* atoms and the cubic phase is the LES for the alloys with larger *C* atoms.

When we compare the experimentally observed GSS of the Co*BC* alloys with our calculated LES (see Table I), we find a very good match between the two, barring a few exceptions such as in CoCrAs, CoFeGe, and CoFeAs. CoFeGe is reported to be synthesized in hexagonal Ni_2In structure ($P6_3/mmc$) [9,42], whereas our calculations show an orthorhombic structure to be the LES. However, it is to be noted that the difference in E_{form} of the hexagonal and the orthorhombic structures (7.67 meV = 0.74 kJ/mol) is within the thermal energy (refer to Table S1 in the Supplemental Material [66]). A similar observation is found in the case of CoFeAs, where the experimentally synthesized hexagonal Fe_2P-type structure [51,52] and our calculated orthorhombic structure have very close values of E_{form} (the difference being 2.07 meV = 0.2 kJ/mol). The difference in E_{form} of the orthorhombic and hexagonal structures is slightly high (32.01 meV = 3.09 kJ/mol), but of the order of thermal energy in the case of CoCrAs, where the reported GSS is hexagonal ($P\bar{6}2m$) [51,52], unlike our calculated orthorhombic LES. These differences might be due to the fact that as the intermetallic alloys are synthesized in an elevated temperature, the most stable structure may not necessarily be the LES obtained from calculations carried out at 0 K.

2. *Structural stability of* Ni*BC half-Heusler alloys*

The results of the geometric study on the Ni*BC* alloys are presented in Table II. The calculated lattice parameters of the LES match well with the lattice parameters of the experimental GSS (wherever available), the values being within an error bar of about 3%. Among the Ni*BC* alloys,

TABLE II. Number of valence electrons per formula unit (Z_v). Space group of the calculated LES of Ni*BC* alloys: cubic ($F\bar{4}3m$), hexagonal ($P6_3/mmc$ and $P\bar{6}2m$), and orthorhombic ($Pnma$). μ_T and SP are the calculated total spin magnetic moment and the spin polarization of the LES, respectively. The space group of the experimentally observed structure is shown along with the lattice parameter and total spin magnetic moment.

Calculation						Experiment		
Material	Z_v	Space group	Lattice parameter (a, b, c) (Å)	μ_T (μ_B)	SP	Space group	Lattice parameter (a, b, c) (Å)	μ_T (μ_B)
NiCrAl	19	***Pnma***	(4.96, 4.13, 7.31)	2.17	2.8			
NiMnAl	20	***P6$_3$/mmc***	(4.13, 5.13)	3.20	47			
NiFeAl	21	***Pnma***	(4.96, 3.88, 7.49)	2.48	55.5			
NiCrGa	19	***P6$_3$/mmc***	(4.16, 5.08)	2.35	9.4			
NiMnGa	20	***P6$_3$/mmc***	(4.13, 5.18)	3.26	38.5	$P6_3/mmc$ [41]	(4.163, 5.298) [41]	
NiFeGa	21	***P6$_3$/mmc***	(4.11, 5.05)	2.64	60.5			
NiCrSi	20	***P$\bar{6}$2m***	(5.88, 3.62)	2.30	4.4	$Pnma$ [47]		
NiMnSi	21	***Pnma***	(5.85, 3.56, 6.89)	2.83	57.1	$Pnma$ [47]		
NiFeSi	22	***Pnma***	(5.46, 3.63, 6.87)	1.72	71.2	$Pnma$ [47]		
NiCrGe	20	***P$\bar{6}$2m***	(6.07, 3.73)	2.79	26.5			
NiMnGe	21	***Pnma***	(6.01, 3.67, 7.11)	2.98	43.3	$Pnma$ [43,45]		
						$P6_3/mmc$ [43,45]	(6.05, 3.75, 7.09) [45]	
NiFeGe	22	***P6$_3$/mmc***	(4.08, 5.10)	2.37	59.8	$P6_3/mmc$ [9,42]	(4.01, 5.07) [42]	0.5 [42]
NiMnSn	21	***P6$_3$/mmc***	(4.38, 5.47)	3.49	35.2			
NiCrP	21	***Pnma***	(5.85, 3.53, 6.82)	2.62	46.7	$Pnma$ [51,52,56]	(5.79, 3.53, 6.81) [56]	2.36 [56]
NiMnP	22	***P$\bar{6}$2m***	(5.85, 3.46)	2.33	48.4	$Pnma$ [50–52]	(5.95, 3.56, 6.83) [51]	
						$P\bar{6}2m$ [51,52]	(5.94, 3.52) [51]	
NiFeP	23	***P$\bar{6}$2m***	(5.83, 3.36)	1.08	69.7	$P\bar{6}2m$ [50–52]	(5.84, 3.43) [50]	
NiCrAs	21	***Pnma***	(6.14, 3.68, 7.10)	2.99	69.6	$P\bar{6}2m$ [51,52]	(6.10, 3.65) [51]	
NiMnAs	22	***P$\bar{6}$2m***	(6.17, 3.68)	3.44	8.9	$Pnma$ [51–53]	(6.24, 3.79, 7.06) [51]	
						$P\bar{6}2m$ [51–53]	(6.19, 3.72) [51]	
NiFeAs	23	***P$\bar{6}$2m***	(6.03, 3.62)	2.08	57.2	$P\bar{6}2m$ [51,52]	(6.07, 3.58) [51]	
NiCrSb	21	***F$\bar{4}$3m***	(5.89)	3.05	81.6			
NiMnSb	22	***F$\bar{4}$3m***	(5.90)	4.00	100	$F\bar{4}3m$ [9]	(5.92) [9]	3.85 [9]
NiCrS	22	***P$\bar{6}$2m***	(5.89, 3.59)	2.40	5.6			
NiMnS	23	***P$\bar{6}$2m***	(5.95, 3.65)	3.60	21.8			
NiFeS	24	***Pnma***	(5.64, 3.50, 7.21)	2.00	21.6			
NiMnSe	23	***F$\bar{4}$3m***	(5.77)	4.96	78.3			
NiMnTe	23	***F$\bar{4}$3m***	(6.01)	4.87	9.8			

the cubic structure is the LES for those cases, which contain C elements with high atomic number (Se, Sb, and Te) and Z_v value greater than 21. For other C atoms and Z_v values, the noncubic symmetries are the preferred structures. In a recent theoretical study, many of these cubic alloys were reported to show half-metallic-like character in the cubic $C1_b$ structure [37]. However, only a few NiBC alloys have been experimentally synthesized in the cubic $C1_b$ structure to date (see Table II) [9,58]. In the case of many of the NiBC alloys, the calculated symmetry of the LES matches with the experimentally reported GSS, barring a few exceptions. While NiCrAs is found to exhibit a hexagonal $P\bar{6}2m$ GSS [51,52], our calculations yield an orthorhombic LES. We observe that the difference in formation energies of both these structures is only slightly larger than the thermal energy (see Table S2 in the Supplemental Material [66]). Furthermore, NiCrSi is experimentally observed to be in orthorhombic structure [47]. On the other hand, from our calculation the LES is found to possess hexagonal symmetry, $P\bar{6}2m$. However, the formation energy of the orthorhombic structure is close to that of the hexagonal structure (the difference being 35.43 meV = 3.42 kJ/mol per f.u.). We see from Table S2 [66] that the formation energies for the orthorhombic and the hexagonal structures are reasonably close (within 5 meV/f.u.) to each other for most of the NiBC alloys.

3. *Structural stability of* PtBC *half-Heusler alloys*

In the case of PtBC alloys also, the lattice parameters calculated for the LES match well with the experimental value of the GSS (wherever available); the values are within an error bar below 5% (Table III). Except for PtMnGe and PtFeSn, the GSS and LES are the same for the rest of the cases (Table III). However, the differences in E_{form} are found to be rather close (the maximum difference being in the case of PtFeSn) [66]. It is interesting to note here that, among the PtBC alloys, PtCrSn is the special case where both the hexagonal and orthorhombic

TABLE III. Number of valence electrons per formula unit (Z_v). Space group of the calculated LES of PtBC alloys: cubic ($F\bar{4}3m$), hexagonal ($P6_3/mmc$ and $P\bar{6}2m$), and orthorhombic ($Pnma$). μ_T and SP are the calculated total spin magnetic moment and the spin polarization of the LES, respectively. The space group of the experimentally observed structure is shown along with the lattice parameter and total spin magnetic moment.

Calculation						Experiment		
Material	Z_v	Space group	Lattice parameter (a, b, c) (Å)	μ_T (μ_B)	SP	Space group	Lattice parameter (a, b, c) (Å)	μ_T (μ_B)
PtCrAl	19	$\boldsymbol{P6_3/mmc}$	(4.34, 5.50)	3.23	30.4			
PtMnAl	20	$\boldsymbol{P6_3/mmc}$	(4.35, 5.41)	3.51	39.2	$P6_3/mmc$ [9,40]	(4.33,5.50) [9]	
PtFeAl	21	$\boldsymbol{Pnma}$	(5.17, 4.05, 7.93)	2.55	64.8			
PtCrGa	19	$\boldsymbol{P6_3/mmc}$	(4.34, 5.59)	3.28	36.8			
PtMnGa	20	$\boldsymbol{P6_3/mmc}$	(4.36, 5.54)	3.79	35.3	$P6_3/mmc$ [9,40]	(4.33, 5.59) [9]	3.15 [9]
						$F\bar{4}3m$ [8]	6.15 [8]	3.18 [8]
PtFeGa	21	$\boldsymbol{P6_3/mmc}$	(4.35, 5.31)	2.87	60.5			
PtCrIn	19	$\boldsymbol{P6_3/mmc}$	(4.61, 5.76)	3.68	18.5			
PtMnIn	20	$\boldsymbol{P6_3/mmc}$	(4.62, 5.71)	4.01	18.5			
PtFeIn	21	$\boldsymbol{Pnma}$	(5.52, 4.63, 7.93)	3.02	64.2			
PtCrSi	20	$\boldsymbol{Pnma}$	(6.11, 3.88, 7.39)	3.08	6.5			
PtMnSi	21	$\boldsymbol{Pnma}$	(6.23, 3.75, 7.34)	3.05	14.9			
PtFeSi	22	$\boldsymbol{Pnma}$	(5.82, 3.85, 7.27)	1.92	46.5			
PtCrGe	20	$\boldsymbol{Pnma}$	(6.17, 3.99,7.65)	3.56	4.9			
PtMnGe	21	$\boldsymbol{Pnma}$	(6.27, 3.90, 7.59)	3.26	0.99	$P6_3/mmc$ [60]		
PtFeGe	22	$\boldsymbol{P\bar{6}2m}$	(6.30, 3.74)	1.99	71.9			
PtCrSn	20	$\boldsymbol{Pnma}$	(5.87, 4.58, 7.93)	3.61	42.7	$P6_3/mmc$ [58]		
PtMnSn	21	$\boldsymbol{F\bar{4}3m}$	(6.22)	3.67	29.5	$F\bar{4}3m$ [8,9]	(6.264) [9]	3.52 [9]
PtFeSn	22	$\boldsymbol{F\bar{4}3m}$	(6.16)	3.53	77.6	$P6_3/mmc$ [58]		
PtCrP	21	$\boldsymbol{Pnma}$	(6.34, 3.72, 7.27)	3.00	66.4			
PtMnP	22	$\boldsymbol{P\bar{6}2m}$	(6.17, 3.63)	2.12	84.2			
PtFeP	23	$\boldsymbol{P\bar{6}2m}$	(6.05, 3.63)	1.18	59.3			
PtCrAs	21	$\boldsymbol{P\bar{6}2m}$	(6.75, 3.65)	3.16	20.7			
PtMnAs	22	$\boldsymbol{F\bar{4}3m}$	(6.02)	4.01	76.5			
PtFeAs	23	$\boldsymbol{P\bar{6}2m}$	(6.32, 3.71)	1.27	61.6			
PtCrSb	21	$\boldsymbol{F\bar{4}3m}$	(6.22)	3.19	70.6	$FO1$ [9]	(6.439) [9]	
PtMnSb	22	$\boldsymbol{F\bar{4}3m}$	(6.23)	4.02	61.9	$F\bar{4}3m$ [8,9]	(6.21) [9]	3.97 [9]
PtFeSb	23	$\boldsymbol{F\bar{4}3m}$	(6.18)	3.57	65.1	$FO1$ [9]	(6.444) [9]	
PtMnSe	23	$\boldsymbol{F\bar{4}3m}$	(6.14)	4.74	25.7			
PtCrTe	22	$\boldsymbol{F\bar{4}3m}$	(6.33)	4.01	95.5			
PtMnTe	23	$\boldsymbol{F\bar{4}3m}$	(6.35)	4.83	8.63			

structures exhibit equal formation energy (−50.16 kJ/mol) and more importantly the hexagonal structure, which is the equally probable calculated LES (Table 3 and Table S3 in the Supplemental Material [66]), matches with the experimentally observed GSS ($P6_3/mmc$). For Pt-based systems also, the cubic phase is the LES for high-Z elements (As, Se, Sn, Sb, and Te) as the C atom and Z_v value greater than 21. However, it is not the favored symmetry when the C atom has a low Z value. For PtBC, many alloys exhibit cubic LES unlike Ni- and Co-based alloys (compare Tables I–III). In the case of the Pt-based alloys, we have further carried out a full geometry optimization including SOC. A negligible difference (maximum of about 1%) has been observed between the lattice parameters obtained with or without SOC. As observed in the case of CoBC and NiBC alloys, there are many Pt-based cases also where two or more phases are close in terms of energy with the LES (difference in E_{form} within 5 meV/f.u.).

In summary, we find that the cubic symmetry is the LES for only 18 alloys (which typically possess larger C atoms and Z_v value greater than 20) and the rest of the alloys have their LES as noncubic phases. The effect of SOC on the structure is negligible in PtBC alloys. Furthermore, the E_{form} values of some typical ABC alloys in two different symmetries are found to be very close to each other. The closeness of E_{form} indicates that both structures are equally likely to be synthesized under certain experimental conditions. Thus, to understand this closeness of the E_{form} between two symmetries in certain materials, next we carry out a detailed analysis of the geometric and electronic structure of some of the typical cases.

B. Analysis of two symmetries with close E_{form}

1. Geometric analysis of two symmetries with close E_{form}

As mentioned above, we find that there are some alloys where the E_{form} values for two structures are surprisingly very close to each other, the difference being within about 1 kJ/mol (10.36 meV) per formula unit (see Tables S1, S2, and S3 of the Supplemental Material [66]). To understand this small difference in the E_{form}, we perform a detailed geometric analysis. Table IV gives the E_{form}, density of the alloys, and the bond distance between two neighboring atoms (d), for two sets of a few typical alloys. In one set, there is an excellent matching of the E_{form} between two symmetries (examples are PtCrIn, PtCrSn, etc.), and in the other set (examples are CoFeAs, NiMnAs, etc.), no such good matching of E_{form} is observed. When two symmetries of a material are close in terms of geometry (i.e., the density and bond distances), the respective E_{form} values are found to be very close to each other. On the other hand, whenever the formation energies are somewhat close for two different symmetries in a material, their geometries are not necessarily close enough.

To elaborate the results of Table IV, we now discuss a typical example, namely, PtCrSn. In this material, the LES ($Pnma$) has an E_{form} value of −50.16 kJ/mol per f.u. and

TABLE IV. Geometric anaylsis: d gives the bond distance in Å; the unit of density is Mg/m^3.

Material	Space group	E_{form}	Density	d (A-B)	d (A-C)	d (B-C)
CoCrGe	$P6_3/mmc$	−23.89	8.20	2.69	2.37, 2.55	2.69
	$Pnma$	−23.76	7.85	2.65, 2.77, 2.79, 2.81	2.33, 2.36, 2.37	2.58, 2.59, 2.63
CoFeAs	$Pnma$	−43.28	8.51	2.76, 2.80	2.25, 2.31	2.38, 2.52, 2.64
	$P\bar{6}2m$	−43.08	8.47	2.72, 2.78	2.26, 2.36	2.42,2.56,2.62
NiMnAl	$P6_3/mmc$	−97.46	6.16	2.71	2.39, 2.57	2.71
	$Pnma$	−97.00	6.18	2.53, 2.64, 2.78,2.93	2.41, 2.44, 2.54, 2.58	2.63, 2.64, 2.72, 2.95
NiCrGa	$P6_3/mmc$	−29.92	7.88	2.72	2.40, 2.54	2.72
	$Pnma$	−29.80	7.89	2.70, 2.71, 2.72, 2.73	2.40, 2.40, 2.54, 2.54	2.70, 2.71, 2.72, 2.73
NiMnAs	$P\bar{6}2m$	−73.01	7.75	2.77, 2.88	2.35, 2.41	2.55, 2.62
	$Pnma$	−71.66	7.67	2.75, 2.85, 2.90, 2.91	2.34, 2.36, 2.42,2.69	2.56, 2.60, 2.69
PtMnAl	$P6_3/mmc$	−184.86	10.38	2.85	2.51, 2.71	2.85
	$Pnma$	−184.47	10.58	2.71, 2.82, 2.86	2.55, 2.59, 2.67, 2.68	2.69, 2.77, 2.80
PtCrIn	$P6_3/mmc$	−30.08	11.24	3.03	2.66, 2.88	3.03
	$Pnma$	−30.06	11.31	3.00, 3.00, 3.04, 3.04	2.66, 2.66, 2.88, 2.88	3.03, 3.03, 3.03, 3.03
PtMnIn	$P6_3/mmc$	−70.14	11.48	3.03	2.67, 2.86	3.03
	$Pnma$	−70.11	11.48	3.00, 3.00, 3.04, 3.04	2.67, 2.67, 2.86, 2.86	3.02, 3.03, 3.03, 3.03
PtFeIn	$Pnma$	−23.77	12.00	2.96,2.96,3.01, 3.01	2.66,2.66, 2.76, 2.76	2.99, 2.99, 2.99, 3.00
	$P6_3/mmc$	−23.72	12.00	2.99	2.66, 2.76	2.99
PtMnGe	$P\bar{6}2m$	−88.20	11.47	2.84, 3.01	2.46, 2.55	2.70, 2.73
	$Pnma$	−88.04	11.56	2.88, 2.99	2.44, 2.50, 2.60	2.61, 2.65, 2.84
PtCrSn	$Pnma$	−50.16	11.41	3.02, 3.02, 3.03, 3.03	2.64, 2.64, 2.94, 2.94	3.02, 3.02, 3.02, 3.03
	$P6_3/mmc$	−50.16	11.41	3.02	2.64, 2.94	3.02
	$F\bar{4}3m$	−36.02	10.01	2.70	2.70	3.12
	$P\bar{6}2m$	−8.03	10.83	3.03, 3.24	2.63, 2.68	2.90, 2.90, 2.91
PtMnSn	$P6_3/mmc$	−75.29	11.65	3.02	2.66, 2.86	3.02
	$Pnma$	−75.22	11.65	3.00,3.00, 3.03, 3.03	2.66,2.66, 2.86, 2.86	3.02, 3.02, 3.02, 3.02
PtMnSb	$Pnma$	−33.71	11.44	3.02,3.02, 3.06,3.06	2.68,2.68,2.89, 2.89	3.04,3.04, 3.05,3.05
	$P6_3/mmc$	−33.61	11.44	3.05	2.68,2.90	3.05

density value of 11.41 Mg/m^3; the $P6_3/mmc$ symmetry has the same values for these two quantities (−50.16 kJ/mol per f.u. and 11.41 Mg/m^3, respectively), which makes practically both these structures the LES in the case of this material. It is observed that the nearest-neighbor distances and the bond angles (not shown in Table IV) between neighboring atoms are very similar in these two structures. It is also clear from Table IV that the other two symmetries ($F\bar{4}3m$ and $P\bar{6}2m$) are not only energetically farther from the LES, but these are also different from the geometric point of view. A similar result is observed in all the other Ni- and Pt-based systems (see Table IV for some typical examples). Since the density and bond distances (and bond angles) in some of the cases mentioned in Table IV match so well, the internal local geometries of each atom and subsequently the bonding nature in the two phases are the *same*. Furthermore, when the simulated x-ray diffraction (XRD) patterns of the two symmetries with similar local environment are analyzed (Fig. S1 [66]), it is observed that the positions and intensity ratios of different XRD peaks are similar in both structures, although the planes themselves (as assigned in Fig. S1 [66]), of course, are different, as expected. Furthermore, the lattice parameters and the crystallographic fractional coordinates (see Table S4 in the Supplemental Material [66]) are such that the resultant Cartesian coordinates are found to be similar in these two different symmetries ($P6_3/mmc$ and $Pnma$). This indicates that the internal relative arrangements of the atoms in these two structures are identical irrespective of the symmetry (as seen from Fig. S2 [66]).

Next we discuss one of the cases where the E_{form} value of one symmetry is only somewhat close to the LES. We take the example of NiMnAs. The LES $P\bar{6}2m$ has an E_{form} value of −73.01 kJ/mol per f.u. and density value of 7.75 Mg/m^3; the $Pnma$ symmetry has only somewhat close values for these two quantities (−71.68 kJ/mol per f.u. and 7.67 Mg/m^3, respectively). Consequently, the geometric data of the two phases do not exhibit good matching with each other (see Table IV). The comparison of simulated XRD patterns, given in Fig. S1 [66], also indicates a large difference in the position and ratio of intensity of the diffraction peaks for the two structures. Furthermore, the combination of lattice parameters and the crystallographic fractional coordinates (see Table S5 in the Supplemental Material [66]) is such that it results in significantly different Cartesian coordinates and hence different internal relative arrangements of the atoms in these two different symmetries.

2. Analysis of density of states of two symmetries with close E_{form}

Now we analyze the density of states (DOS) of a few typical materials belonging to the two sets mentioned above. Figures 1(a)–1(d) show the total as well as partial DOS of a few materials: PtCrIn, PtCrSn, NiMnAs, and CoFeAs, respectively. For PtCrIn and PtCrSn, two symmetries ($P6_3/mmc$ and $Pnma$) yield very close E_{form} values and also geometry (see Table IV) within our calculational accuracy. As the local environments are similar, the overlapping of the wave functions is expected to result in similar valence-band (VB) DOS. From further analysis of the DOS of the PtCrSn case (shown in Fig. S3 [66]), we find that the DOS of the semicore levels are slightly different (in terms of intensity and/or position of the peaks), although the E_{form} and the VB DOS are the same for two different structures. On the contrary, when the E_{form} for one phase is slightly different compared to the other (as in the case of CoFeAs and NiMnAs), the positions and intensities of different peaks in the VB DOS are not so much alike as seen in the case of PtCrIn and PtCrSn (Fig. 1). Though in the cases of NiMnAs and CoFeAs, the E_{form} is different by only about 0.5 kJ/mol, it is seen from Figs. 1(c) and 1(d) that the matching of the DOS of these two phases is not excellent.

After the discussion of stability, the next two sub-sections are devoted to detailed analysis of the magnetic as well as electronic properties (total and partial DOS) of the cubic and noncubic phases of the alloys to understand the similarities and differences in their properties. Our main motivations of these analyses are to find (1) why 100% SP at the E_F is often associated with cubic symmetry in the literature, and (2) whether a noncubic ground state of a HHA may exhibit very high or even 100% SP at E_F.

C. Magnetic and electronic properties of the cubic *ABC* half-Heusler alloys

1. Magnetic moment and spin polarization of the cubic ABC half-Heusler alloys

In Tables I–III, we present the number of valence electrons per formula unit (Z_v), the total spin magnetic moment, and the SP of the alloys in the LES. In all these materials, the Z_v are found to be from 21 to 23. Furthermore, these alloys assume a ferromagnetic (FM) configuration, where the moments of both the atoms A and B orient along the same direction (see Tables S6, S7, and S8 [66]). Among the 18 stable cubic alloys (a flow chart of these stable alloys is shown in Fig. S4 [66]), 10 possess close to integral total spin magnetic moment. The total moments of these alloys are found to be exactly or very close to $3\mu_B$, $4\mu_B$, and $5\mu_B$ for Z_v values of 21, 22, and 23, respectively. This means that the spin magnetic moment scales linearly with the atomic number (Z) of any of the atoms (A or B or C) in ABC half-metallic alloys. In all these cases discussed here, the B atom carries the maximum moment [66]. Figure 2(a) shows the total spin magnetic moment as a function of Z_v of the energetically stable CoBC, NiBC, and PtBC alloys. For CoMnSb, CoMnTe, and NiMnSb alloys, the total magnetic moment follows the Slater-Pauling rule [7,21]. The calculated total spin magnetic moments of these cubic alloys are in close agreement with the results reported in the literature, wherever available [3,6,7,14,21–24,28–30,32,33,35–37].

Now we discuss the SP at E_F of the materials which exist in cubic LES. From Fig. 2(b), it is observed that only CoMnSb, CoMnTe, and NiMnSb exhibit 100% SP, which matches with the literature [3,7]. Furthermore, CoMnSe and PtCrTe possess close to 100% SP. It is to be noted here that most of the CoBC materials possess high SP (above 60%) in the cubic case. For NiBC, only with the exception of NiMnTe, all the cubic cases exhibit high SP (above 80%). However, for PtBC, SP for PtMnSn, PtMnSe, and PtMnTe are found to be below 50%; the rest are above 50%, with only one being close to 100%.

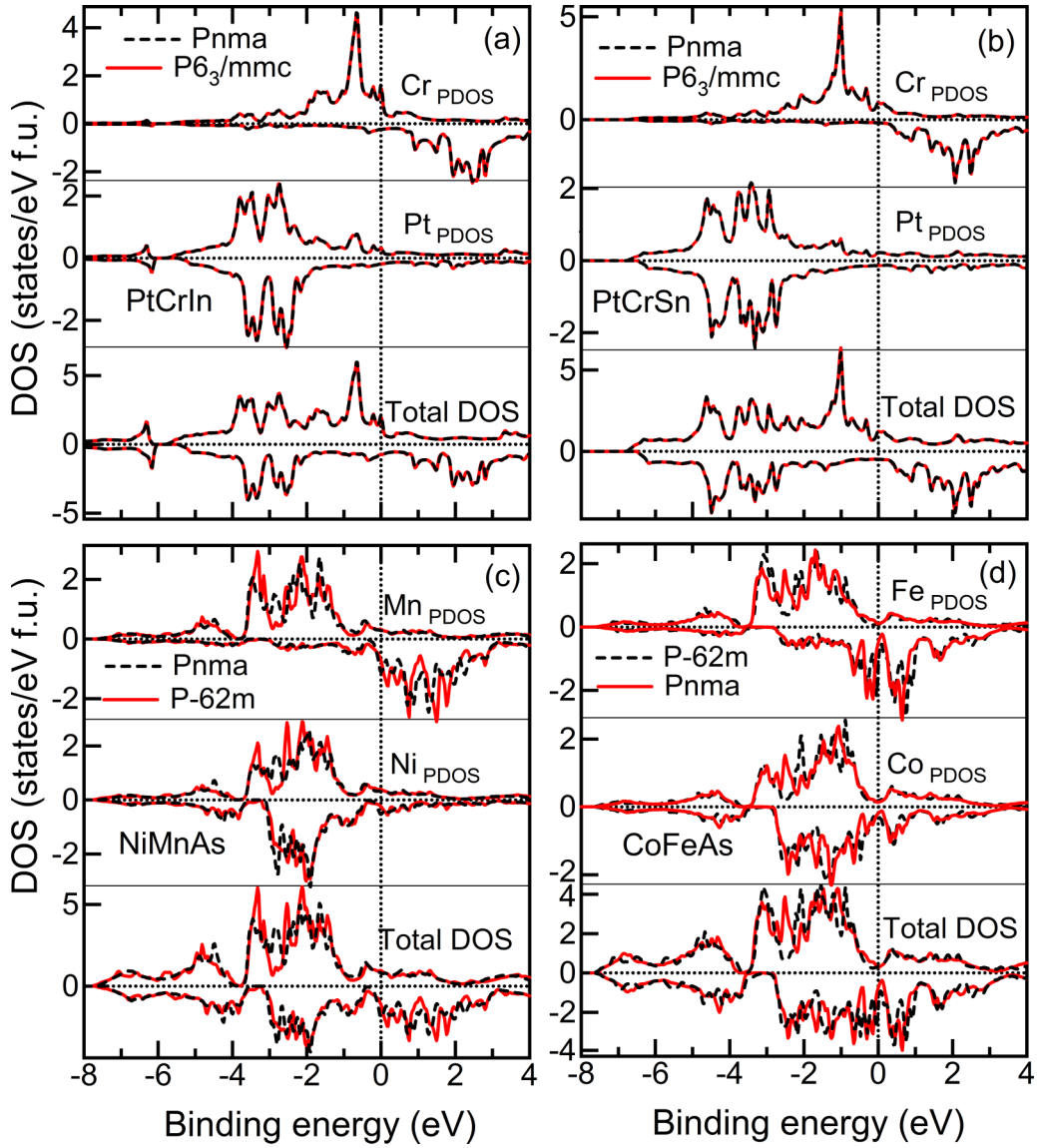

FIG. 1. The total DOS and partial DOS of *A* and *B* atoms, for a few alloys, (a) PtCrIn, (b) PtCrSn, (c) NiMnAs, and (d) CoFeAs, for which two symmetries yield close values of E_{form} and also geometry. The DOS of the lowest energy phase is plotted with a solid (red) line and the DOS of the other phase is plotted with a (black) dashed line.

2. DOS and band structure of the cubic ABC half-Heusler alloys

Many of the cubic *ABC* half-Heusler alloys are known to be half-metallic in nature. In a half-metal, electrons close to E_F determine the half-metallic gap and contribute to the transport properties. Therefore, it is important to understand the nature of the DOS at the E_F as well as in the valence band. For overall comparison of the electronic structure, we calculate the spin-polarized total and partial DOS as well as the band structure of the Co*BC*, Ni*BC*, and Pt*BC* alloys in cubic LES.

Co*BC*. First we discuss in detail the electronic structure of Co*BC* alloys. To elaborate the similarities and differences in the DOS and band structures of these alloys, we present the results of electronic structure for CoMnSb, CoMnSe, CoMnTe, CoFeSb, and CoFeTe alloys in Figs. 3(a)–3(e), respectively. The electronic structure of CoMnSb, CoFeSb, and CoMnTe alloys has been reported in the literature and our calculated data match well with these results [7,35].

From the analysis of the DOS, we observe that, as the number of valence electrons of the *C* atom increases in a period (Sb to Te), the VB width increases systematically from about 6 to 7 eV. This is primarily due to the shifting of the *sp* states of the *C* atom away from the E_F. On the other hand, the peak positions corresponding to the *3d* states of *A* and *B* atoms remain the same. Subsequently, there is an overall shift of the VB DOS towards higher binding energy. On the contrary, when the number of valence electrons of the *B* atom increases in a period (from Mn to Fe), the overall VB width remains almost the same. However, there is a shift of the position of the *3d* DOS of the transition metals towards higher binding energy. A similar observation is found in case of Ni*BC* and Pt*BC* alloys also. When the *A* atom changes, namely, the Co

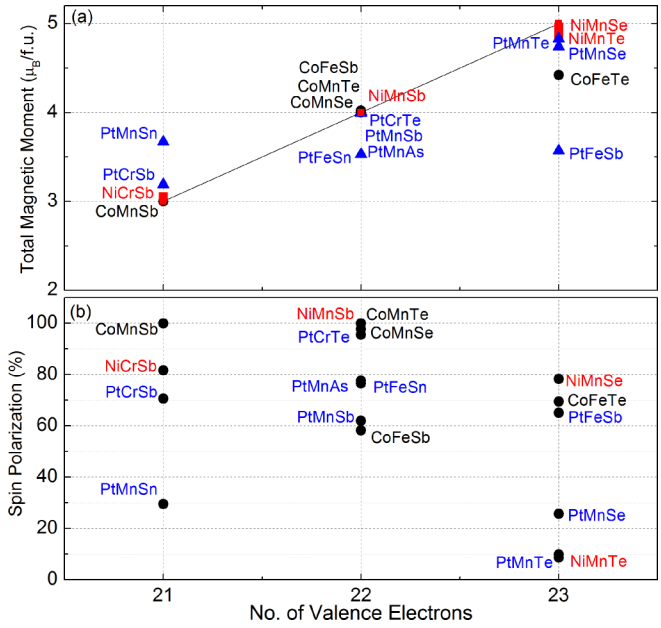

FIG. 2. The total moment and SP of the Co*BC*, Ni*BC*, and Pt*BC* cubic LES as a function of total number of valence electrons per formula unit.

atom is replaced by Ni and Pt, the shifting of the weight of the DOS towards higher binding energy is observed.

Now we discuss the spin-polarized DOS (atom and orbital-projected) and band structure of Co*BC* alloys. In the case of CoMnSb, CoMnSe, and CoMnTe [shown in Figs. 3(a)–3(c)], the VB mainly consists of hybridized Co and Mn *3d* states and the *p* states of the *C* atom. The *s* states of the *C* atom lie well below the E_F, as expected. It is observed that, in these alloys, the spin-up VB DOS corresponds to the hybridized Co and Mn *3d* states, whereas the same for spin-down states mostly corresponds to the Co *3d* states. Very close to E_F, the spin-up DOS primarily corresponds to the $3d_{e_g}$ and $3d_{t_{2g}}$ states of the Co atom as well as the $3d_{t_{2g}}$ states of the Mn atom. At higher binding energies, the contribution of the Co and Mn $3d_{t_{2g}}$ states is large, whereas the $3d_{e_g}$ states are present in the intermediate binding energy range. The gap in the spin-down DOS of CoMnSb and CoMnTe appears mainly between the occupied bonding and unoccupied antibonding $3d_{t_{2g}}$ levels of the Mn atom in these alloys. The origin of the band gap in the spin-down band of half-metallic HHAs has already been discussed in the literature and has been associated with the hybridization between the two transition-metal elements [7,21]. We find that, in CoMnSb, the E_F lies just above the spin-down VB maximum, with the spin-down band gap of about 0.87 eV and a half-metallic gap of about 0.05 eV. This calculated value of the band gap is in close agreement with the value reported in the literature [35,37]. In case of CoMnSe, the E_F lies exactly in the middle of the spin-down band gap of about 0.9 eV and the half-metallic gap is about 0.46 eV. In the minority band structure, an electronlike pocket is observed at the Γ point. Although the total spin magnetic moment is an integer and a gaplike nature is present in the spin-down DOS, the material does not show proper half-metallicity since analysis of the band structure indicates crossing of a single band in the spin-down case. Hence, this material is rather likely to behave as a semimetal. Consequently we note that the SP is calculated to be 97.8% in the case of CoMnSe. In the isoelectronic CoMnTe, the E_F lies almost in the middle of the spin-down band gap of about 1.06 eV (indirect band gap) and the half-metallic gap is about 0.38 eV. In the literature, Lin *et al* studied the half-metallic property of CoMnTe HHA by first-principles calculations [35]. They found that CoMnTe is the most robust half-metallic ferromagnet with a band gap and half-metallic gap of 1.13 and 0.42 eV, respectively. Therefore, our results match well with the literature. Furthermore, we note that, as the Z_v increases from 21 (in CoMnSb) to 22 (in CoMnTe), the width of the spin-down band gap and half-metallic gap increases. This indicates that the stability of the half-metallic system increases. Similarly, for the isoelectronic alloys CoMnSe and CoMnTe, as the size of the *C* atom increases, from the DOS it is observed that the spin-down gap (gaplike nature in the case of CoMnSe) increases. Therefore, the CoMnTe system is expected to be more stable.

When the *B* atom changes from Mn to Fe, the width of the VB slightly increases (by about 0.8 eV in CoFeSb as compared to CoMnSb). Although the overall VB DOS is similar in both materials, a slight difference is observed near the E_F. In CoFeSb [shown in Fig. 3(d)], the spin-up DOS at E_F is primarily contributed by $3d_{t_{2g}}$ states of the Co atom, and has a small contribution from Co $3d_{e_g}$ as well as Fe $3d_{t_{2g}}$ states. Unlike CoMnSb, where the E_F lies at the top of the spin-down DOS in the VB, E_F lies almost at the bottom of the unoccupied conduction band in the case of CoFeSb. A spin-down gap of about 0.41 eV is present below E_F in CoFeSb. Although CoFeSb seems to be half-metallic from band structure, with an indirect band gap of about 0.7 eV and half-metallic gap of about 0.6 eV, there is a finite spin-down DOS at the E_F. Hence, CoFeSb is metallic with a SP value of 58.3%. It is to be noted here that the spin magnetic moment ($3.9793\mu_B$) and SP (52.37%) of CoFeSb calculated by Ma *et al.* [37] match closely with our calculated values ($5.99\mu_B$ and 58.3% in Table I). The overall nature of the VB DOS of CoFeTe [shown in Fig. 3(e)] is similar to that of CoFeSb with a slightly higher DOS at the E_F in the former case. A spin-down gap of about 0.63 eV is present below the E_F. To date there is no literature available on the theoretical work of CoFeTe, which is predicted to be metallic from our calculations. If we look at the band structure of all the Co*BC* alloys, we find that the minority bands just below the E_F are less dispersive compared to the majority bands. This indicates that the hybridized spin-down *3d* states are reasonably localized near E_F.

Ni*BC*. We now discuss the spin-polarized VB DOS and band structure of four Ni*BC* alloys, i.e., NiCrSb, NiMnSb, NiMnSe, and NiMnTe in Figs. 4(a)–4(d), respectively. In the NiCrSb alloy, it is observed that the VB width is about 6.5 eV and it consists of hybridized Ni and Cr *3d* states. A large peak near E_F in the spin-up DOS is due to the $3d_{e_g}$ and $3d_{t_{2g}}$ states of both Ni and Cr atoms. However, at higher binding energy, the spin-up DOS is primarily contributed by both the $3d_{e_g}$ and $3d_{t_{2g}}$ states of Ni and $3d_{t_{2g}}$ states of Cr. The spin-down DOS mainly corresponds to the $3d_{e_g}$ and $3d_{t_{2g}}$ states of Ni. A spin-down gap of about 0.41 eV is present well above E_F. From our calculation, NiCrSb is found to be metallic [however, with a rather small DOS at the spin-down channel as seen from Fig. 4(a)] and the calculated spin magnetic moment

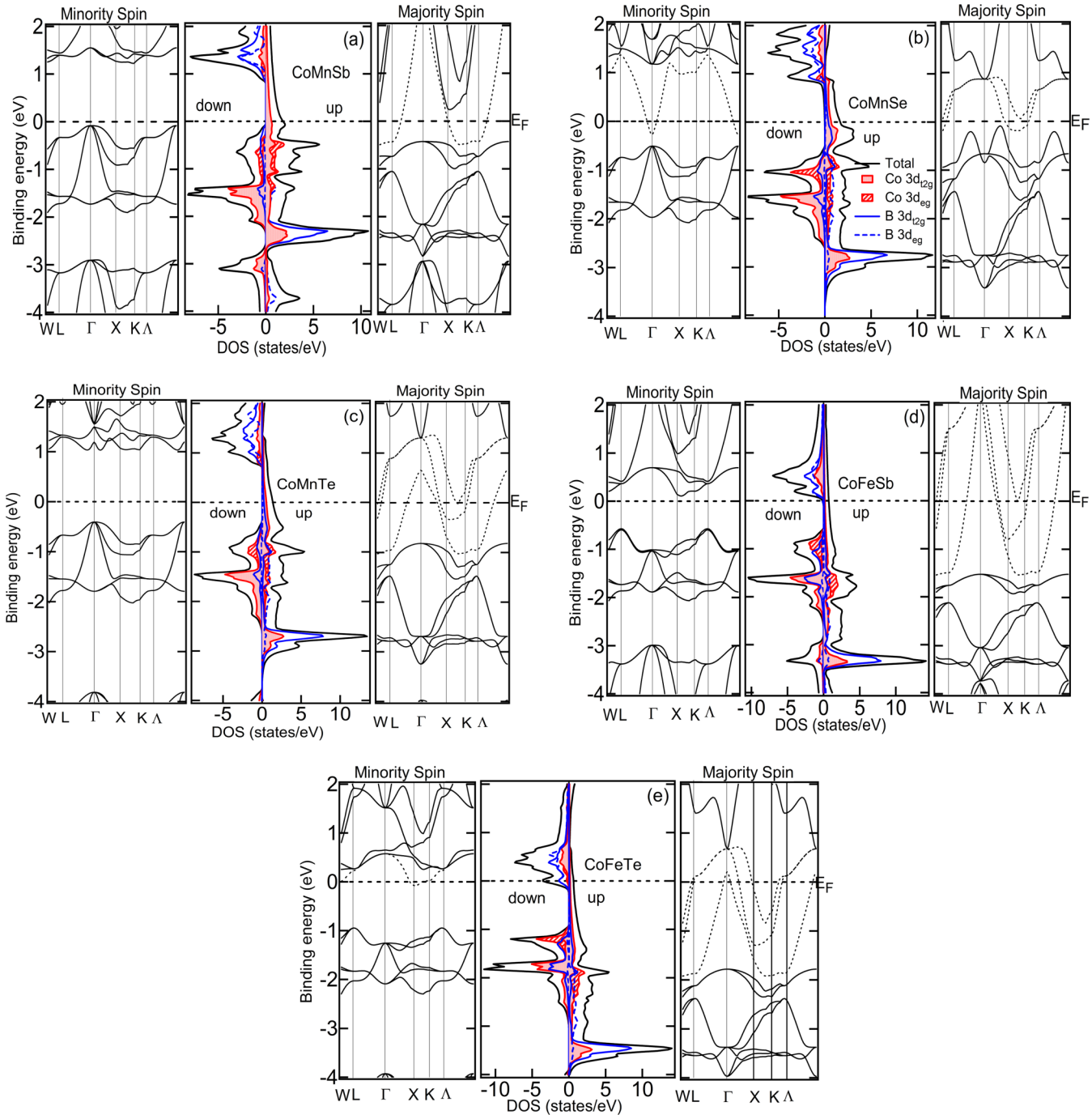

FIG. 3. The spin-polarized total DOS and band (plotted with a solid black line) as well as atom projected DOS of Co*BC* alloys: (a) CoMnSb, (b) CoMnSe, (c) CoMnTe, (d) CoFeSb, and (e) CoFeTe in the cubic LES. The atom projected DOS of the Co atom is plotted with red color (solid filled pattern for Co $3d_{t_{2g}}$; and hashed pattern for Co $3d_{e_g}$) and that of the *B* atom is plotted in blue solid (*B* $3d_{t_{2g}}$) and dashed lines (*B* $3d_{e_g}$). The bands which cross the E_F are plotted in dotted lines (black).

($3.05\mu_B$) is slightly larger than the value ($2.994\mu_B$) reported by Zhang *et al.* [22], but it matches well with the value ($3.0598\mu_B$) calculated by Dinh *et al.* [29]. In contrast to that, from the first-principles electronic structure calculations using the full-potential linearized augmented plane-wave method based on DFT, NiCrSb has been predicted to be a half-metallic system with a gap of 0.38 eV by Ghimire *et al.* [30]. The spin magnetic moment was reported to be $3.01\mu_B$ by these authors which, however, is close to our value of $3.05\mu_B$ (Table II).

When the *B* atom is changed from Cr to Mn, the width of the VB remains unchanged. For NiMnSb, in the spin-up channel [Fig. 4(b)], the DOS at E_F and at higher binding energy are primarily contributed by $3d_{t_{2g}}$ states of Ni and Mn, whereas the states close to E_F are contributed by $3d_{e_g}$ and $3d_{t_{2g}}$ states of Ni and Mn. In NiMnSe and NiMnTe [Figs. 4(c) and 4(d)], also the overall nature of VB is similar to NiMnSb. The half-metallic gap is about 0.15 eV and the spin-down gap is about 0.46 eV for NiMnSb which matches

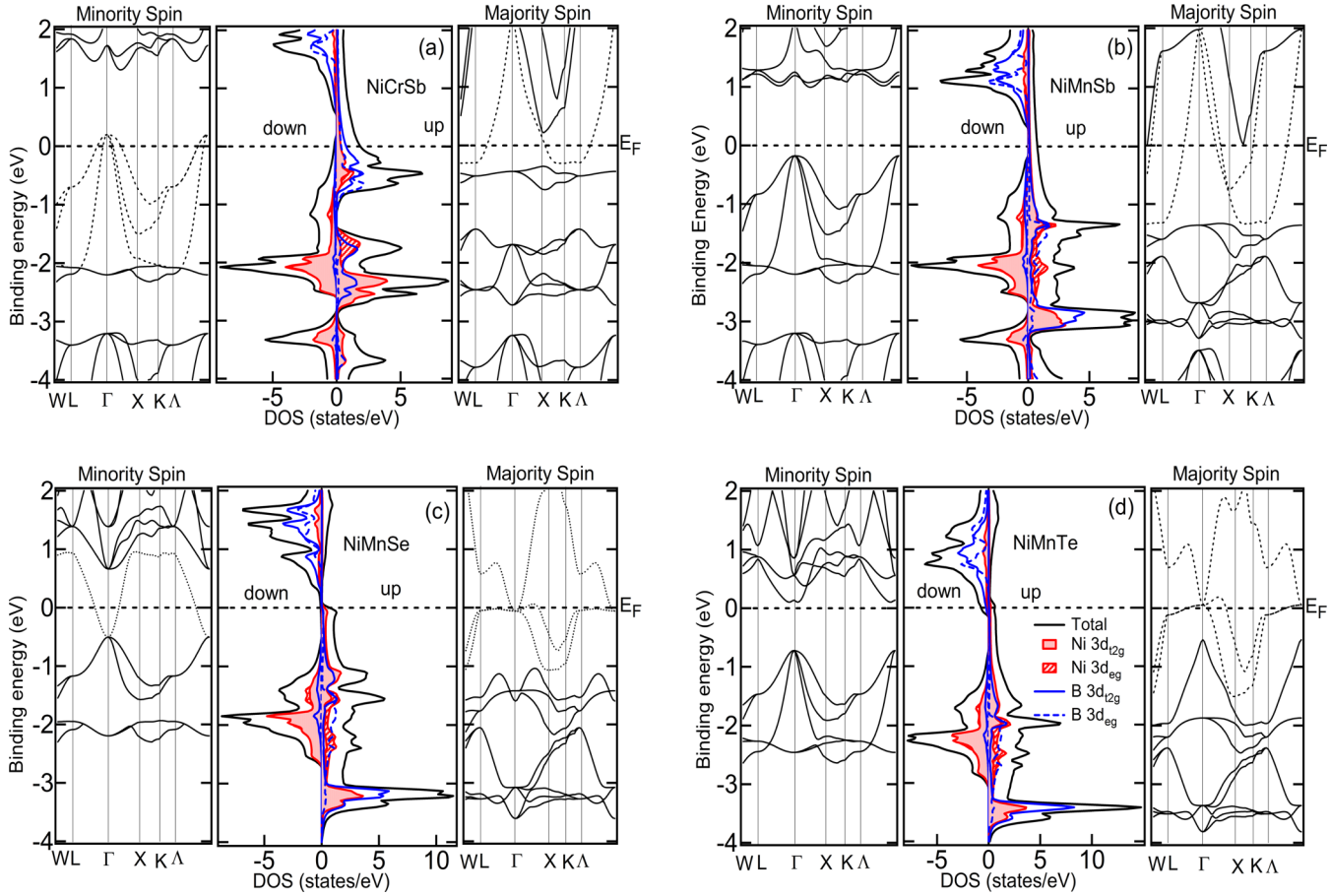

FIG. 4. The spin-polarized total DOS and band (plotted with a solid black line) as well as atom projected DOS of Ni*BC* alloys: (a) NiCrSb, (b) NiMnSb, (c) NiMnSe, and (d) NiMnTe in the cubic LES. The atom projected DOS of the Ni atom is plotted with red color (solid filled pattern for Ni $3d_{t_{2g}}$; and hashed pattern for Ni $3d_{e_g}$) and that of the *B* atom is plotted in blue solid (*B* $3d_{t_{2g}}$) and dashed lines (*B* $3d_{e_g}$). The bands which cross the E_F are plotted in dotted lines (black).

with the literature [7,23,30,32,33,37]. When the *C* atom is changed to Se from Sb, the VB width increases to about 7.5 eV and the spin-down gap of about 0.24 eV is present below E_F. In the isoelectronic alloy NiMnTe, the VB width is similar to NiMnSe and a spin-down gap of about 0.52 eV is observed below E_F. From our calculated DOS we find that both NiMnSe and NiMnTe are metallic in nature. However, there is no literature available to validate our results.

The band structure of the four Ni*BC* alloys are also shown in Figs. 4(a)–4(d). In the VB of NiCrSb, one highly dispersive spin-up band (which is in the conduction band) and three spin-down bands crossed the E_F at more than one *k* point. In NiMnSb, triply degenerate and highly dispersive spin-up bands cross E_F at more than one *k* point and there is a gap in the spin-down band. In the band structure of NiMnSe, three highly dispersive spin-up bands just touch the E_F at more than one *k* point and one spin-down band which is in the conduction band crossed the E_F at three *k* points. In NiMnTe, two highly dispersive spin-up bands cross the E_F at more than one *k* point and there is an indirect band gap in the spin-down band along this particular *k* direction as mentioned in Fig. 4(b). It is to be noted here that, although NiMnTe shows metallic behavior (from the spin-polarized DOS), it exhibits a half-metallic property along this specific *k* path.

From the detailed analysis of magnetic and electronic properties of the Co*BC* and Ni*BC* alloys in their cubic LES phase, we find that only three materials, CoMnSb, CoMnTe, and NiMnSb, show 100% spin polarization. It is important to check the robustness of the half-metallic property of these alloys against lattice distortion for practical applications. Hence, we probe here the effect of volume-conserving tetragonal distortion on the half-metallicity. Figures 5(a), 5(d), and 5(g) show the calculated energy difference between the tetragonally distorted phase and the cubic structure (at its equilibrium lattice parameter) as a function of c/a ratio in case of CoMnSb, CoMnTe, and NiMnSb HHAs, respectively. It is observed that for these alloys, the tetragonal structure is energetically higher than the cubic phase. Furthermore, with tetragonal distortion, the SP value reduces significantly after a certain value of c/a ratio in all three cases. The percentage change of SP and the energy gap in the spin-down DOS at different values of c/a ratio are shown in Figs. 5(b), 5(e), and 5(h), and Figs. 5(c), 5(f), and 5(i), respectively, for CoMnSb, CoMnTe, and NiMnSb HHAs. For CoMnSb, the half-metallic property is completely destroyed with tetragonal distortion. Furthermore, the half-metallic property is retained only for a small value of tetragonal distortion for the other

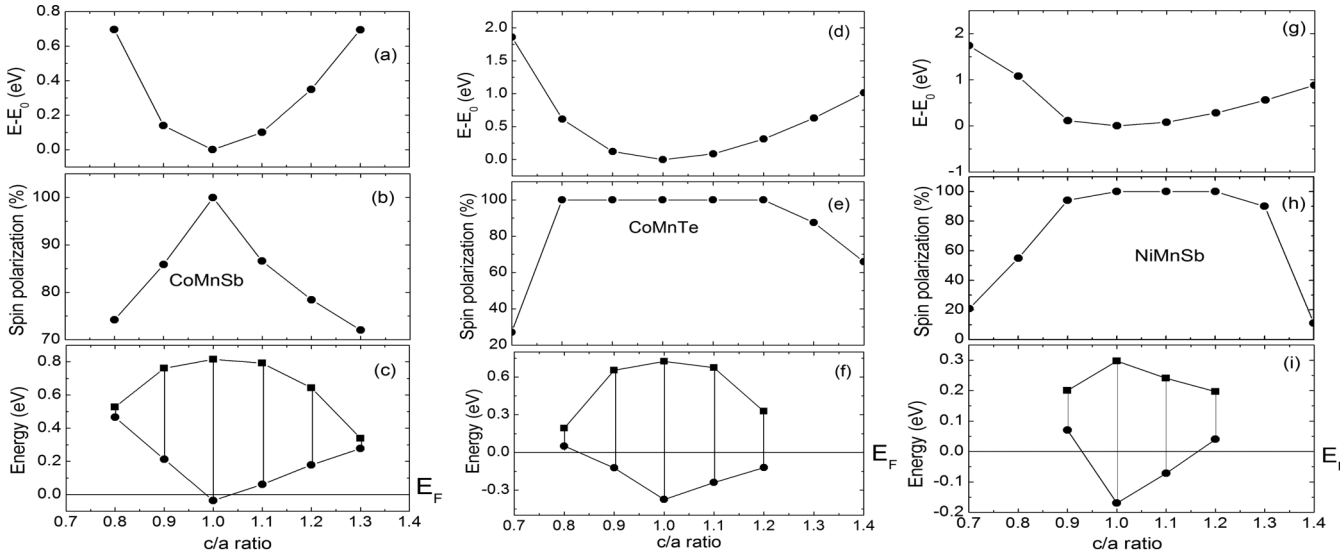

FIG. 5. The energy difference between the tetragonal distortion and the cubic structure at its equilibrium lattice parameter as a function of c/a ratio of (a) CoMnSb, (d) CoMnTe, and (g) NiMnSb HHAs. The spin polarization at different c/a ratio of (b) CoMnSb, (e) CoMnTe, and (h) NiMnSb HHAs. The energy gap in the spin-down DOS at different c/a ratio of (c) CoMnSb, (f) CoMnTe, and (i) NiMnSb HHAs. Solid circles and solid squares represent the valence-band maximum and the conduction-band minimum in the spin-down DOS at the same c/a ratio, respectively. E_F is located at 0 eV and indicated by the horizontal solid line.

two materials (i.e., a c/a ratio of 0.8 to 1.2 for CoMnTe and 1.0 to 1.2 for NiMnSb).

Pt*BC*. There are only a few theoretical studies available in the literature for Pt-based alloys [3,7,14,24,36]. Hence, we discuss in detail the electronic structure of some newly predicted Pt*BC* alloys in cubic LES (PtCrTe, PtMnAs, PtMnSe, PtMnTe, and PtFeSn) along with the others already available in the literature (PtCrSb, PtMnSb, PtMnSn, and PtFeSb). From our first-principles calculations, we find that the Pt-based cubic LES alloys are primarily metallic in nature [see Figs. 6(a)–6(h)]. From the comparison of the DOS of PtCrSb and PtCrTe, we find that the VB width of the Te-based alloy is larger (about 7.08 eV) compared to the Sb case (about 6.3 eV). In both the alloys, near E_F, the spin-up DOS mainly corresponds to the $3d_{e_g}$ and $3d_{t_{2g}}$ states of Cr with a small contribution from the $5d_{e_g}$ and $5d_{t_{2g}}$ states of Pt. At higher binding energy, the spin-up DOS is primarily contributed by the $5d_{e_g}$ and $5d_{t_{2g}}$ states of Pt. Furthermore, the spin-down DOS is primarily contributed by $5d_{e_g}$ and $5d_{t_{2g}}$ states of Pt. A spin-down gap of about 0.60 eV is found above E_F in the conduction band in PtCrSb. In the literature, from first-principles calculations based on DFT using the full potential local orbital method, within the GGA and local spin-density approximation (LSDA), PtCrSb has been found to be metallic in nature [36], which matches with our study. However, it is shown to exhibit half-metallicity at nearly 27 GPa pressure within the GGA [36].

When the *C* atom belongs to the same group, for example, in the case of PtMnAs and PtMnSb, the VB width is seen to be almost similar (about 6.6 eV). Near E_F, the spin-up DOS consists of mainly the $3d_{t_{2g}}$ states of Mn with a small contribution from $5d_{t_{2g}}$ and $5d_{e_g}$ states of the Pt atom in PtMnAs. However, in PtMnSb, near E_F, the spin-up DOS consists of mainly the $3d_{t_{2g}}$ and $3d_{e_g}$ states of Mn with a small contribution from $5d_{t_{2g}}$ and $5d_{e_g}$ states of Pt (as observed in PtCrSb and PtCrTe). At higher binding energy the spin-up DOS is primarily contributed by the $5d_{t_{2g}}$ states of Pt in both materials.

PtMnSb has been extensively studied in the literature; however, the results of band structure of this material are found to be somewhat controversial. Our calculated results are in line with some and differ from the other studies. From the band-structure calculation by de Groot *et al.*, using the augmented-spherical-wave method, PtMnSb is found to be fully half-metallic in nature. The electronic structure of PtMnSb has also been studied by Ebert *et al.* using the linear muffin-tin-orbital method of band-structure calculation [14]. The result of their calculations is in agreement with the earlier study. Using first-principles, self-consistent tight-binding linear-muffin-tin-orbital calculations within the atomic-sphere approximation, it has been shown that PtMnSb shows half-metallicity [24]. All these above-mentioned results are in contradiction with our finding. Furthermore, the calculated moment of this alloy has also been found to be slightly lower than our calculated value. From the full-potential linear muffin-tin orbitals method calculations, Galanakis *et al.* showed that the spin-down gap is above E_F [7]. We note here that the electronic properties of PtMnSb and PtCrSb have been investigated by Habbak *et al.* using first-principles calculations based on DFT with the full potential local orbital (FPLO) method and the GGA as well as the LSDA have been used as the exchange-correlation potential [36]. They found that PtMnSb is half-metallic with a spin-down gap of 0.83 eV and spin magnetic moment of $4\mu_B$ using the LSDA. However, it is not found to be half-metallic within the GGA. On the other hand, PtMnSb has been shown to turn into a half-metallic alloy at nearly a pressure of 6 GPa using the GGA. Our calculation (which is also based on the full

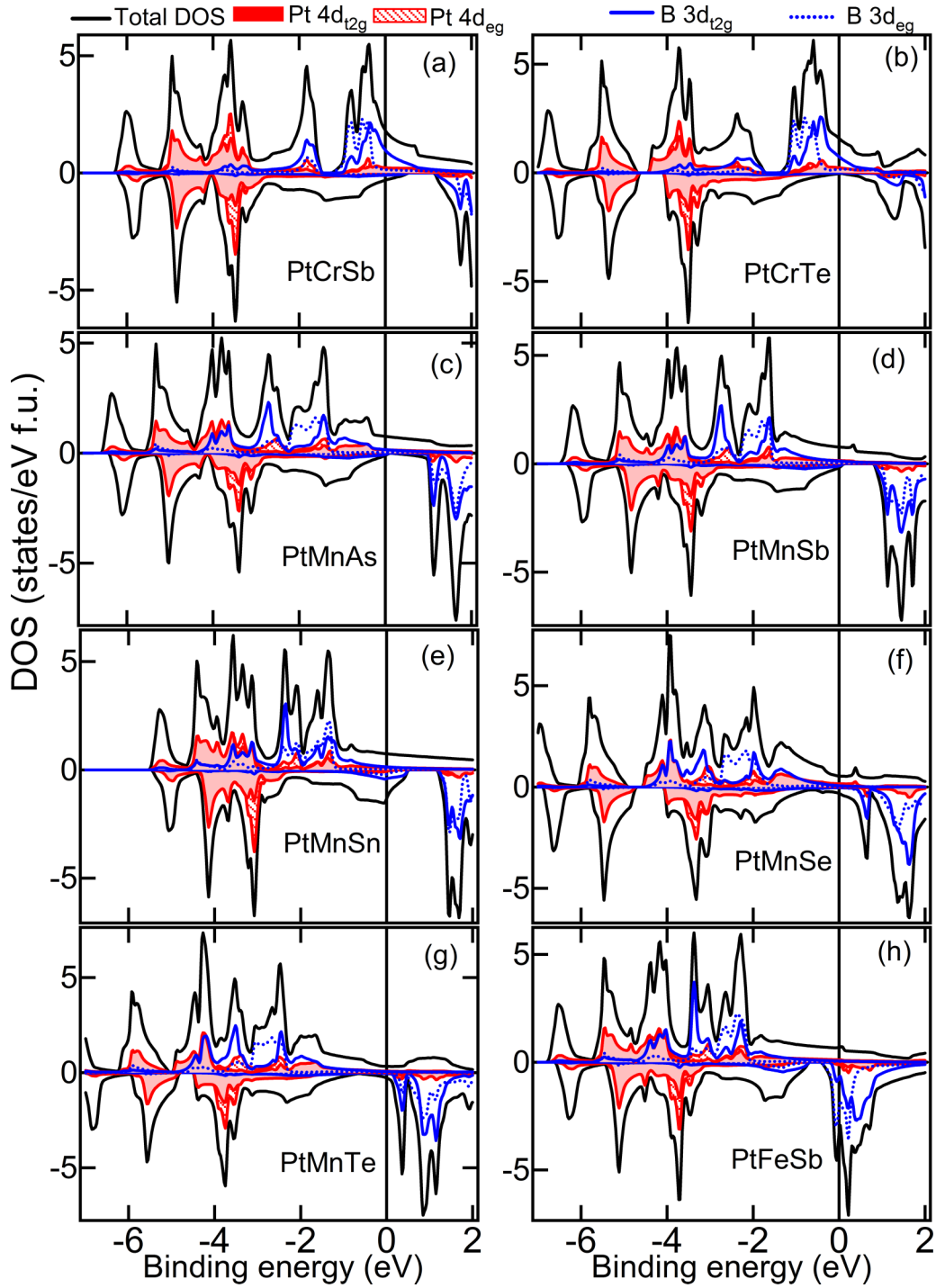

FIG. 6. The spin-polarized total DOS and the atom projected DOS of Pt*BC* alloys (a) PtCrSb, (b) PtCrTe, (c) PtMnAs, (d) PtMnSb, (e) PtMnSn, (f) PtMnSe, (g) PtMnTe, and (h) PtFeSb in the cubic LES without including spin-orbit interaction. The total DOS are plotted with a solid line (black). The atom projected DOS of the Pt atom is plotted with red color (solid filled pattern for Pt $4d_{t_{2g}}$; and hashed pattern for Pt $4d_{eg}$) and that of the *B* atom is plotted in blue solid (*B* $3d_{t_{2g}}$) and dashed lines (*B* $3d_{e_g}$).

potential method) is in close agreement with the two reports mentioned above [7,36].

In the case of PtMnSn, the reported literature [3,24] as well as our calculations show this alloy to be metallic in nature with large spin-down DOS at E_F. In the case of PtMnTe, the VB has a width of about 7.6 eV. At E_F, there is a large spin-up and a small spin-down DOS. Near E_F, the spin-up DOS consists of mainly the $d_{t_{2g}}$ and d_{e_g} states of both Mn and Pt. In PtFeSn, the VB of width about 6.0 eV consists of hybridized Pt and Fe $d_{t_{2g}}$ and d_{e_g} states. E_F lies in the large spin-down and a small spin-up DOS. The spin-up DOS consists of mainly the $d_{t_{2g}}$ and d_{e_g} states of Fe and Pt. The spin-down DOS is primarily contributed by $5d_{t_{2g}}$ and $5d_{e_g}$ states of Pt. Near E_F, the spin-down DOS consists of $3d_{t_{2g}}$ and $3d_{e_g}$ states of Fe and small $5d_{e_g}$ states of Pt. E_F lies within the large spin-down DOS which consists of mainly $d_{t_{2g}}$ and d_{e_g} states of Fe. The spin-

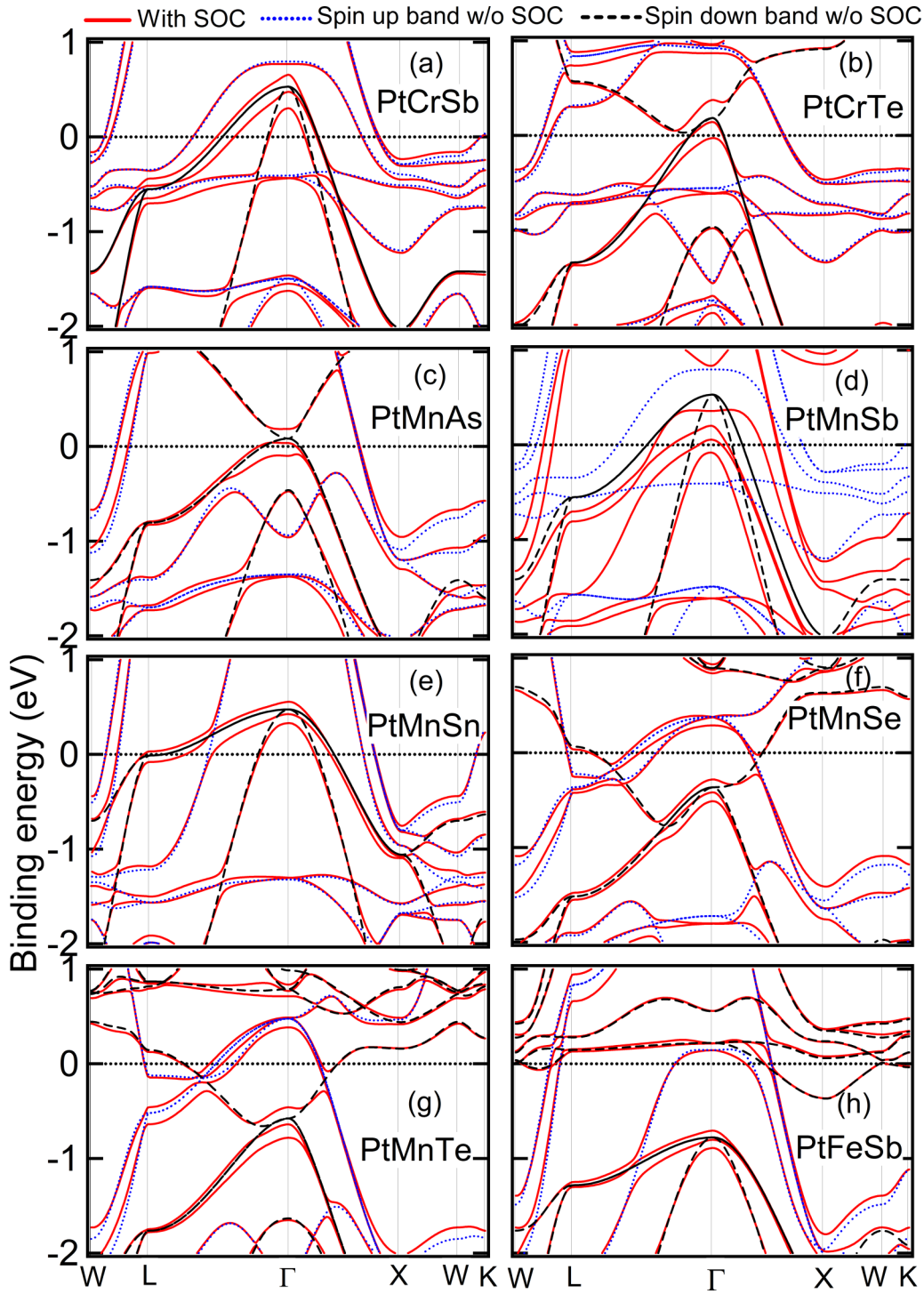

FIG. 7. The band structure of Pt*BC* HHAs with and without including spin-orbit interaction. The spin-up and spin-down bands without spin-orbit interaction are plotted with a dotted line (blue) and dashed line (black), respectively. The bands with spin-orbit interaction are plotted with a solid line (red).

down band with gap of about 0.35 eV is seen to be present below the E_F.

As Pt is a high-Z element, it is expected that the effect of SOC may have some significance in the geometric and electronic structure of Pt*BC* alloys. To explore this, we have also calculated the DOS and band structure of Pt-based alloys by including SOC, after geometry optimization using SOC. By comparing the total DOS calculated with and without SOC, no significant changes have been observed at and around E_F; only the total DOS is shifted to higher binding energy as compared to the DOS calculated without including SOC. Similarly there is no significant contribution from the orbital moment to the total magnetic moment, when SOC is included. The maximum values of orbital magnetic moments are of the order of $0.05\mu_B$ for Pt, $0.1\mu_B$ for B, and $0.005\mu_B$ for C atoms.

Now we discuss the band structure of Pt*BC* alloys with and without including SOC, which is shown in Figs. 7(a)–7(h). In the case of PtCrSb, triply degenerate spin-down bands (calculated without SOC) are present above the E_F. When SOC is included, the degeneracy of these bands is lifted and the bands split into three with almost equal energy spacing and the maxima of all the bands are above E_F. Hence, by including SOC no half-metallic character is induced in PtCrSb. In fact PtCrSb behaves as a metal as found from calculations both with and without SOC. In PtCrTe, a doubly degenerate spin-down band (without SOC), which is present above the E_F, splits into two when SOC is included. One of these bands is shifted below E_F and the other is above the E_F. In the case of PtMnAs, a similar effect is observed as in PtCrTe. For PtMnSb, the effect of SOC near E_F is significant. In the presence of SOC, the triply degenerate spin-down bands present above the E_F are split in such a way that one band is below E_F and other two are above E_F. For PtMnSn, the spin-down bands are above the E_F when SOC is included. In the case of PtMnSe and PtMnTe, the spin-down bands which are present below the E_F (without SOC) split slightly and shift below the E_F when SOC is included. For PtFeSb the splitting is not found to be significant. The effect of SOC on spin-up bands is found to be negligible in all the alloys. From the analysis of band structure we find that all the Pt-based alloys are metallic with or without including SOC. From the band-structure calculations by Youn *et al.*, PtMnSb is found to be metallic when SOC is taken into account in the calculation [5]. To date no detailed band-structure calculations either with or without SOC exist for the other Pt-based alloys in the literature.

In summary, we observe that many, not all, of the materials show a half-metallic property in their cubic phase, but only three materials (CoMnSb, CoMnTe, and NiMnSb), as evident from our calculations, show 100% SP at E_F in their LES. It is probed and found that this half-metallicity is somewhat robust (except in the case of CoMnSb) under volume-conserving tetragonal distortion. However, it is to be noted that this leads to a higher energy state of the materials.

D. Magnetic and electronic properties of the noncubic *ABC* half-Heusler alloys

1. Magnetic moment and spin polarization of noncubic ABC half-Heusler alloys

Now we discuss the total and partial spin magnetic moments and also the spin polarization at E_F. In the literature, many Co*BC*, Ni*BC*, and Pt*BC* HHAs are theoretically predicted to be half-metallic in the cubic structure [21–37]. Our calculated results are largely in agreement with the existing literature. However, in experiments, most of these alloys, such as ternary transition-metal silicides, germanides, phosphides, and arsenides, are synthesized in either hexagonal $P6_3/mmc$ or $P\bar{6}2m$ or orthorhombic *Pnma* structures. Since there is no systematic work on the magnetic, electronic, and half-metallic properties of various alloys in the noncubic phases, our motivation is to study any similarities and differences in these properties through theoretical calculations. Furthermore, we would also like to explore if we can predict from the *ab initio* calculations any novel noncubic half-metallic HHAs.

In Tables I–III (as well as in Tables S6, S7, and S8 [66]) we show the results of calculated spin magnetic moment and SP at E_F of the noncubic *ABC* HHAs to analyze the magnetic properties in detail. In Figs. S5 and S6, we show the total spin magnetic moment in the orthorhombic and the hexagonal ($P6_3/mmc$ and $P\bar{6}2m$) LES as a function of Z_v. Unlike the cubic cases, no systematic increasing trend of total moment with increase in Z_v is observed for the noncubic LES. For Co*BC* alloys, where the maximum number of alloys are likely to form in the orthorhombic phase, it is seen from Fig. S5 that the spin magnetic moment shows a maximum value when *B* is a Mn atom. Furthermore, in this phase, when the *Z* value of the *C* atom increases, the total moment increases. It is seen that, for the hexagonal LES (Fig. S6), the total moment value increases with increase in the Z_v value of the *C* atom. From the analysis of partial moments we find that in most of the cases the moments on the *B* and *C* atoms are antiparallel to each other (Tables S6 to S8 in the Supplemental Material [66]) and the moments on the latter atoms are much smaller compared to the earlier ones, as is observed in the cubic phase as well. Furthermore, in the majority of the cases the moments on the *A* and *B* atoms are found to be parallel to each other. Our calculated total spin magnetic moment values are in good agreement with the reported literature [9,50,53,56]. From Tables I–III we identify many alloys which exhibit close to integral spin magnetic moment and/or reasonably high SP. Hence, to study the magnetic and electronic properties in a systematic way, we have classified the noncubic LES alloys into four categories (see the flow chart in Fig. 8).

Category 1. In this category, we have listed the noncubic Co*BC*, Ni*BC*, and Pt*BC* alloys which are experimentally synthesized and their experimental GSS is the same as the calculated noncubic LES. Additionally, these alloys show 100% SP in the theoretically calculated cubic $C1_b$ phase. Some of the typical examples are discussed here. In CoCrP and CoMnP, the calculated total spin magnetic moment in their orthorhombic LES is somewhat close to the integral values of $1.93\mu_B$ and $2.99\mu_B$, respectively. While CoCrP possesses a reasonably high SP of 76.3%, CoMnP has an SP of 13.8%.

Category 2. Under this category we have considered those alloys which do not show half-metallicity in the cubic phase, and their calculated noncubic LES matches with the experimentally synthesized GSS. Specific examples are NiFeP (respective total moment and SP are $1.08\mu_B$ and 69.7% in $P\bar{6}2m$ LES), NiFeAs (total moment is $2.08\mu_B$ and SP is 57.2% in $P\bar{6}2m$ LES), CoFeSi (total moment is nonintegral $2.56\mu_B$ and SP is 66% in *Pnma* LES), NiFeSi (total moment is $1.72\mu_B$ and SP is 71.2% in *Pnma* LES), NiFeGe (total moment is $2.37\mu_B$ and SP is 59.8% in $P6_3/mmc$ LES), CoFeP (total moment is close to integral $2.04\mu_B$ and SP is 23.3% in *Pnma* LES), and NiMnGe (total moment is close to integral $2.98\mu_B$ and SP is 43.3% in *Pnma* LES).

In categories 3 and 4, we have listed a few alloys which are not yet synthesized in any experiment.

Category 3. These alloys show half-metallicity in the cubic phase, but their LES is noncubic. Some of these alloys show high SP and some show low SP in their LES. For example, NiFeGa (SP=60.5%), PtMnP (SP=84.2%), and PtFeGa (SP=60.4%) are the alloys in this category which exhibit high

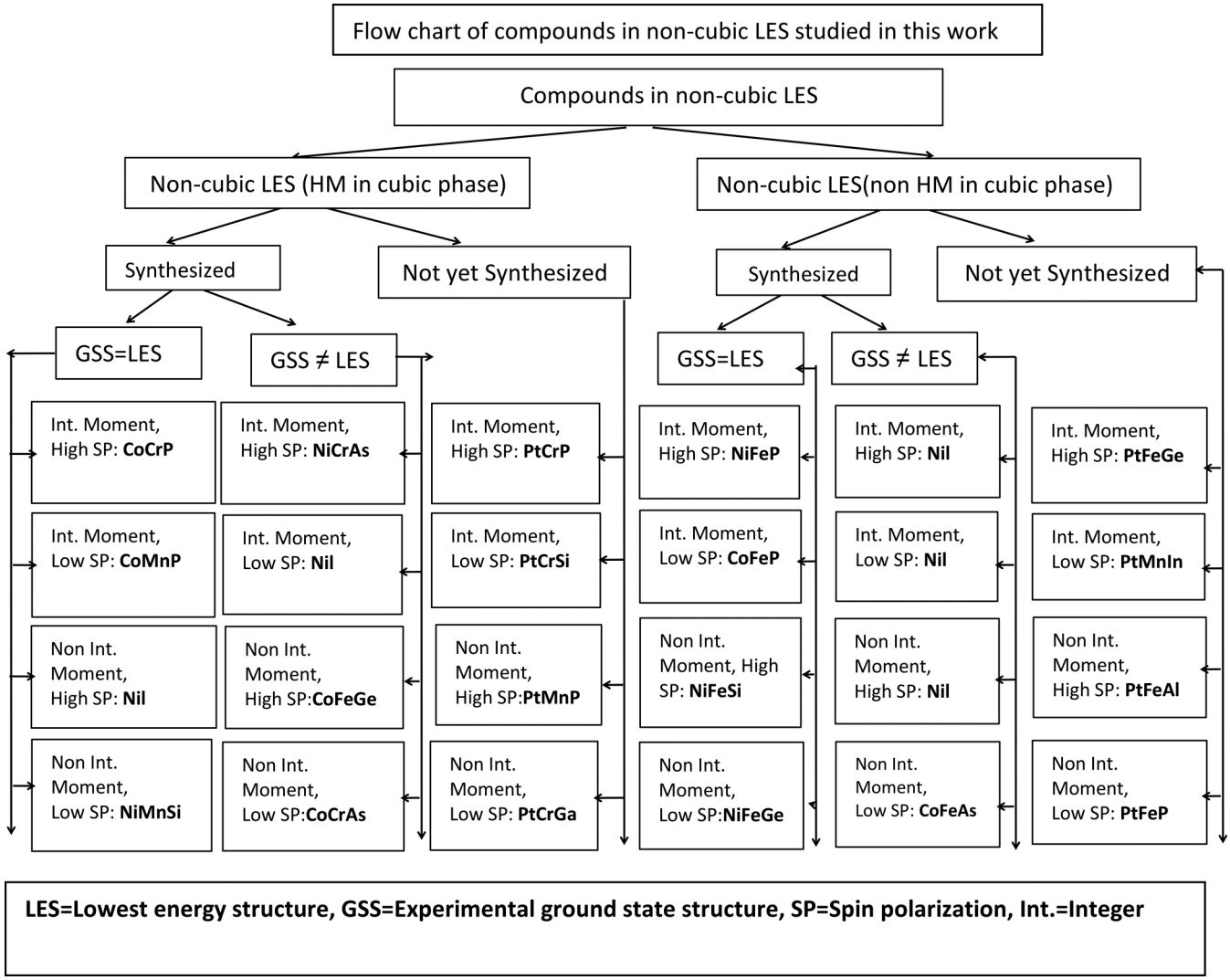

FIG. 8. Flow chart showing the stability of noncubic compounds.

SP (greater than 60%) although the total spin magnetic moment is nonintegral. Furthermore, PtCrP and PtFeIn possess close to integer moment values of $3.00\mu_B$ and $3.02\mu_B$ and SP values of 66.4% and 64.2%, respectively. On the other hand, PtCrSi has a total moment of $3.08\mu_B$ which is somewhat close to integral value, but it possesses a very small SP value of 6.5%.

Category 4. These alloys do not show half-metallicity in the cubic phase and their LES is noncubic. Some specific examples where the SP is high in the LES but the moment value is nonintegral are PtFeAl (total moment is $2.55\mu_B$ and SP is 64.8% in *Pnma* LES), PtFeP (total moment is $1.18\mu_B$ and SP is 59.3% in $P\bar{6}2m$ LES), and PtFeAs (total moment is $1.27\mu_B$ and SP is 61.6% in $P\bar{6}2m$ LES); all these have high SP. However, though the following materials show close to integer moment values, a few of them show low SP, for example, PtMnIn (total moment $4.01\mu_B$ and SP is 18.5% in $P6_3/mmc$ LES), PtMnSi (total moment is $3.05\mu_B$ and SP is 14.9% in *Pnma* LES), NiFeS (total moment is $2.00\mu_B$ and SP is 21.6% in *Pnma* LES), and CoFeS (total moment is $2.98\mu_B$ and SP is 33.6% in *Pnma* LES), and a few of them show high SP, for example, PtFeGe (total moment is $1.99\mu_B$ and SP is 71.9% in $P\bar{6}2m$ LES).

It is reported in the literature that the cubic HHAs which show the half-metallic property possess integral moment (and hence follow the Slater-Pauling rule), but the reverse is not true; i.e., if the total spin magnetic moment is integral, it does not imply that the alloy behaves like a half-metal. A similar trend is also observed in noncubic alloys. Although a few alloys possess close to integer moment values, none of these exhibit 100% SP. From the analysis of spin magnetic moment and SP, we find that some noncubic alloys with *Pnma* symmetry and $Z_v = 21$ show close to integral moment and tend to follow the Slater-Pauling rule, for example, CoCrSi (*Pnma*, $Z_v - 18 = 0.99$, SP=36.9%), CoCrP (*Pnma*, $Z_v - 18 = 1.93$, SP=76.3%), CoMnP (*Pnma*, $Z_v - 18 = 2.99$, SP=13.8%), NiMnGe (*Pnma*, $Z_v - 18 = 2.98$, SP=43.3%), NiCrAs (*Pnma*, LES, $Z_v - 18 = 2.99$, SP=69.68%), PtFeIn (*Pnma*, $Z_v - 18 = 3.02$, SP=64.2%), PtMnSi (*Pnma*, $Z_v - 18 = 3.05$, SP=14.9%), and PtCrP (*Pnma*, $Z_v - 18 = 3.0$, SP=66.4%). But the alloys listed above may or may not exhibit high SP at E_F as our calculated values of SP (given

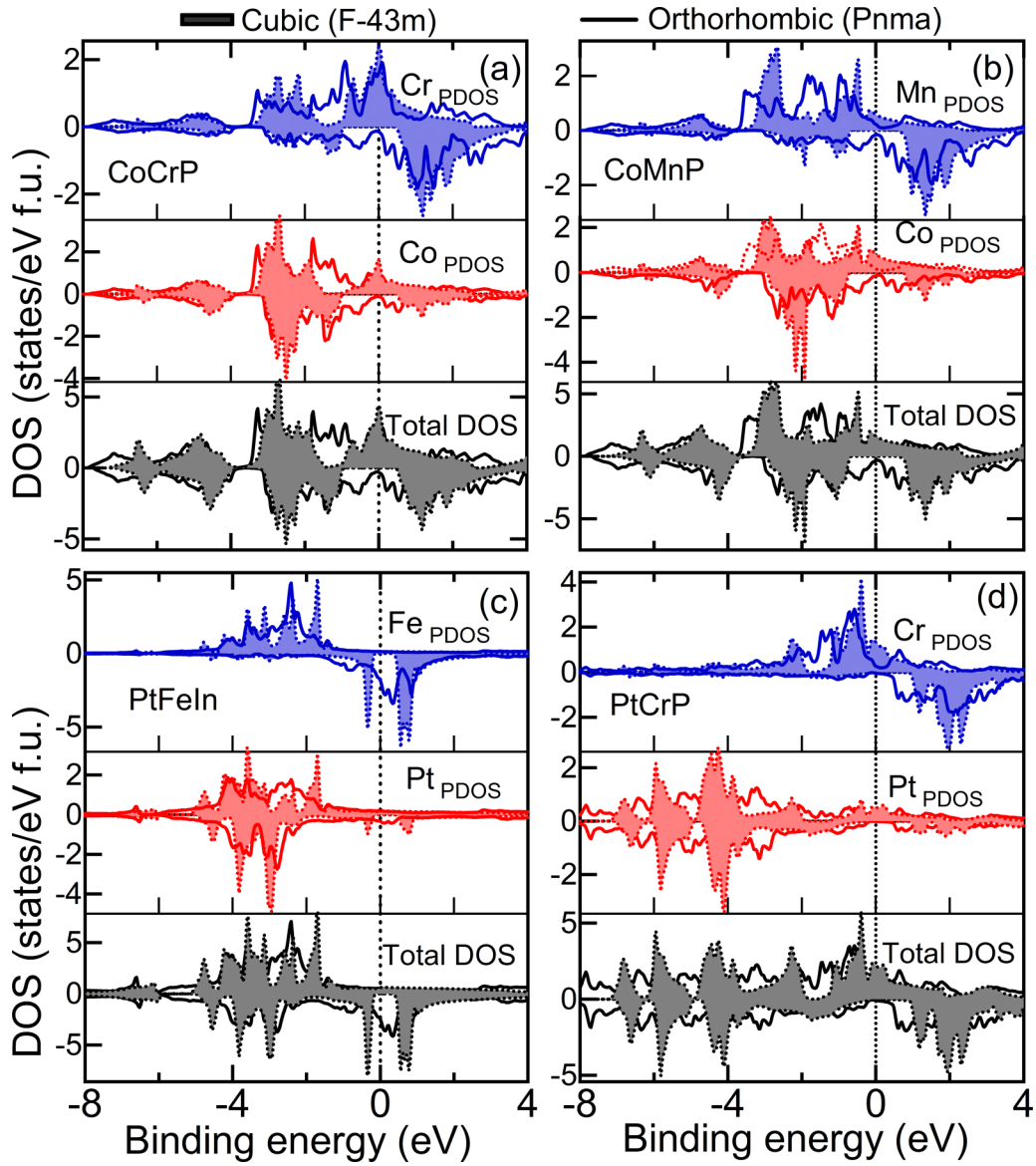

FIG. 9. Comparison of the total and partial (*A* and *B* atoms) DOS of the cubic as well as the noncubic LES (which show close to integer moment and high SP) of the (a) CoCrP, (b) CoMnP, (c) PtFeIn, and (d) PtCrP HHAs. The cubic DOS are shown in solid filled patterns with a dotted outline and the DOS of noncubic LES are shown in solid lines in black (total DOS), red (*A* atom), and blue (*A* atom).

in brackets) clearly show. In the following, we discuss the DOS and band structure of some of the typical cases, which possess close to integral moments and/or high SP at E_F.

2. DOS and band structure of some of the typical cubic ABC half-Heusler alloys

From the analysis of the electronic structure, we find that most of the alloys mentioned in the above four categories are metallic in nature (in LES/GSS) with finite DOS in both spin-up and spin-down bands; the DOS of these alloys are not discussed here. But we concentrate here on the detailed electronic structure of some of those noncubic HHAs, which specifically possess integral moment and show a gap or a pseudogap with a very low DOS at the E_F, for one or both of the spin channels, for example, CoCrP, CoMnP, PtFeIn, and PtCrP (see Fig. 9). In the case of PtCrP in the LES (*Pnma* phase), a very small spin-down DOS at the E_F is observed. The DOS at the spin-up channel is also small but this results in an effective SP at the E_F of about 66% in PtCrP. Contrary to this case, CoMnP behaves somewhat like a semimetal rather than a half-metal since there are small densities of states at both the spin channels, spin-up DOS being just slightly larger in intensity than the spin-down DOS. Furthermore, in case of CoCrP, the spin-down DOS at E_F shows a pseudogap with a high DOS in the spin-up channel. This results in a high value of SP of about 76.3%. The DOS of PtFeIn is quite different compared to the other cases, where the spin-up channel has a negligible DOS and there is a large spin-down DOS at E_F.

In Fig. 9, we have also compared the DOS of these typical alloys in their LES and in the cubic phase. From the analysis of the electronic structure, we observe that the partial DOS

of the transition-metal atoms spread throughout the VB and the effect of crystal field spitting of the *d* orbitals is less in the case of the orthorhombic and hexagonal structures. On the other hand, in the cubic structure of the alloys, the crystal field splitting is significant and the *d* orbitals are relatively localized. Therefore, the absence of a half-metallic gap in the noncubic phase may be attributed to the lack of crystal field splitting and the delocalization of the *d* orbitals. To elaborate about it further, the following discussion may be noted. In the noncubic *Pnma* structure considered in this work, the transition metals *A* and *B*, which have lower *Z* than the *A* atom, occupy the tetrahedral and the pyramidal sites, respectively [50–52]. Since these structures are closely packed, a large orbital overlapping is expected. Because of this overlapping there is a probability of the presence of a dominating metallic character. This leads to the states being delocalized and in turn an absence of band gap in any of the spin channels in the noncubic structures. Now in light of the above, we discuss the relevant electronic structure for the cubic case to elucidate the basic difference between the cubic and noncubic geometrical and electronic structures (Fig. 9). In the ordered cubic HHAs, one of the *A* sublattices is empty and the second *A* atom has a coordination number of 8 (four *A*-*B* and four *A*-*C* bonds in a tetrahedral configuration). The coordination numbers of *B* and *C* are 10, both with octahedral geometry, with four *B*-*A* and six *B*-*C* bonds as well as four *C*-*A* and six *C*-*B* bonds, respectively. Because of the open structure of the cubic symmetry (due to the presence of a void), there is less orbital overlapping and this results in a larger degree of localization of the *d* orbitals. This may be leading to the presence of a spin-down gap in the DOS in this structure (Fig. 9). Therefore, we observe that there is no rigorous one-to-one relationship among the cubic symmetry, integral total moment, and high SP, but a strictly half-metallic behavior (with exactly 100% SP) is found to be associated only with the cubic lowest energy structure.

Finally, by combined analysis of magnetic and electronic structure calculations, only five materials (CoCrP, NiCrAs, NiFeP, PtCrP, and PtMnP alloys) are predicted to be noncubic HHAs with significantly high, but not 100%, SP in their LES. However, the point to be noted here is that a high SP does not necessarily indicate the possibility of semiconducting behavior along one spin channel and, in turn, a possible application of a material as an appropriate spin-injector material. Furthermore, we predict from our present calculations that PtCrP may be the only noncubic material which in its orthorhombic phase may have a potential in this regard since this material is also found to be magnetic in nature. This observation awaits experimental validation.

IV. CONCLUSION

In this work, geometric, electronic, and magnetic properties of Ni-, Co-, and Pt-based half-Heusler alloys, namely, Ni*BC*, Co*BC*, and Pt*BC* (B = Cr, Mn, and Fe; C = Al, Si, P, S, Ga, Ge, As, Se, In, Sn, Sb, and Te) have been calculated in detail using first-principles calculations based on density functional theory. Quite a few of these materials with a *C* atom from groups IIIA, IVA, and VA have already been experimentally and/or theoretically found in various different symmetries. In this work, we probe the stability of all the above-mentioned alloys in different crystal symmetries, reported in the literature. These structures include, the most common (face-centered) cubic $C1_b$ phase (space group $F\bar{4}3m$), and also orthorhombic (space group *Pnma*) as well as hexagonal (space groups $P\bar{6}2m$ and $P6_3/mmc$) phases. We find from our calculations of formation energy that along with alloys with *C* elements from groups IIIA, IVA, and VA, alloys with *C* elements from group VIA are also, by and large, energetically stable. It has also been observed that high-*Z* elements as the *C* atom lead to stabilized phases in the case of the Pt-based alloys. On the contrary, it is not so in the case of Co- and Ni-based materials.

In the literature half-metallicity in many half- and full-Heusler alloys has been shown to exist which is typically associated with a cubic symmetry. We note from our results of the calculated magnetic properties that there is a possibility of the existence of some novel noncubic half-metallic-like half-Heusler alloys, as these possess close to total integer moments. Therefore, to discuss the relative stabilities of different symmetries in order to search for the respective lowest energy state for all the materials as well as to ascertain whether a material is half-metallic or not, we analyze the partial and total density of states. Based on the results of the magnetic and electronic properties, (i) we show that for a material depending on the hybridization between different atoms a particular symmetry is more stable compared to the cubic or other phases; (ii) we observe that there is no rigorous *one-to-one relationship* between the *cubic symmetry* and *high spin polarization at the Fermi level*; (iii) however, it is found that a half-metallic behavior (with 100% spin polarization) is associated only with the cubic symmetry and it is robust under volume-conserving tetragonal distortion in some of the cases (CoMnTe and NiMnSb); and (iv) along with a few new cubic and noncubic half-metallic-like alloys, we predict the possibility of the existence of a novel *noncubic* alloy with a significantly low DOS in one of the spin channels and *high spin polarization at the Fermi level*. PtCrP is this material (magnetic in nature with a moment of $3\mu_B$) with a reasonably high SP at E_F (about 66%) which has been identified in this work.

Furthermore, we have also explored the effect of spin-orbit interaction in the Pt-based alloys. Both from the geometric as well as the electronic structure calculations, we observe that the SOC does not play a crucial role. It has been observed that the inclusion of SOC does not lead to opening up of a half-metallic gap in any of the otherwise metallic alloys.

ACKNOWLEDGMENTS

The authors thank P. A. Naik and Arup Banerjee for facilities and constant encouragement throughout the work. The scientific computing group of the computer center, RRCAT, Indore, and P. Thander are thanked for help in installing and support in running the codes. The authors thank T. Ganguli for constant encouragement and scientific discussion, especially for the detailed discussion on XRD data analysis. M.B. thanks K. Baraik for writing the MATLAB program required for data plotting. D. Pandey is thanked for the discussion during the analysis of VASP data.

[1] S. A. Wolf, D. D. Awschalom, R. A. Buhrman, J. M. Daughton, S. von Molnar, M. L. Roukes, A. Y. Chtchelkanova, and D. M. Treger, Science **294**, 1488 (2001).

[2] I. Zutic, J. Fabian, and S. Das Sharma, Rev. Mod. Phys. **76**, 323 (2004).

[3] R. A. de Groot, F. M. Mueller, P. G. van Engen, and K. H. J. Buschow, Phys. Rev. Lett. **50**, 2024 (1983).

[4] R. A. de Groot and K. H. J. Buschow, J. Magn. Magn. Mater. **54–57**, 1377 (1986).

[5] S. J. Youn and B. I. Min, Phys. Rev. B **51**, 10436 (1995).

[6] V. N. Antonov, P. M. Oppeneer, A. N. Yaresko, A. Ya. Perlov, and T. Kraft, Phys. Rev. B **56**, 13012 (1997).

[7] I. Galanakis, P. H. Dederichs, and N. Papanikolaou, Phys. Rev. B **66**, 134428 (2002).

[8] F. A. Hames and J. Crangle, J. Appl. Phys. **42**, 1336 (1971).

[9] K. H. J. Buschow, P. G. van Engen, and R. Jongebreur, J. Magn. Magn. Mater. **38**, 1 (1983).

[10] P. G. van Engen, K. H. J. Buschow, R. Jongebreur, and M. Erman, Appl. Phys. Lett. **42**, 202 (1983).

[11] R. B. Helmholdt, R. A. de Groot, F. M. Mueller, P. G. van Engen, and K. H. J. Buschow, J. Magn. Magn. Mater. **43**, 249 (1984).

[12] M. J. Otto, H. Feil, R. A. M. van Woerden, J. Wijngaard, P. J. V. Andervalk, C. F. van Bruggen, and A. Haas, J. Magn. Magn. Mater. **70**, 33 (1987), and references therein.

[13] R. A. de Groot, P. G. van Engen, P. P. J van Engelen, and K. H. J. Buschow, J. Magn. Magn. Mater. **86**, 326 (1990).

[14] H. Ebert and G. Schütz, J. Appl. Phys. **69**, 4627 (1991).

[15] J. F. Bobo, P. R. Johnson, M. Kautzky, F. B. Mancoff, E. Tuncel, R. L. White, and B. M. Clemens, J. Appl. Phys. **81**, 4164 (1997).

[16] S. Gardelis, J. Androulakis, P. Migiakis, J. Giapintzakis, S. K. Clowes, Y. Bugoslavsky, W. R. Branford, Y. Miyoshi, and L. F. Cohen, J. Appl. Phys. **95**, 8063 (2004).

[17] T. Block, M. J. Carey, B. A. Gurney, and O. Jepsen, Phys. Rev. B **70**, 205114 (2004).

[18] V. Ksenofontov, G. Melnyk, M. Wojcik, S. Wurmehl, K. Kroth, S. Reiman, P. Blaha, and C. Felser, Phys. Rev. B **74**, 134426 (2006).

[19] Z. Wen, T. Kubota, T. Yamamoto, and K. Takanashi, Sci. Rep. **5**, 18387 (2015).

[20] N. P. Duong, L. T. Hung, T. D. Hien, N. P. Thuy, N. T. Trung, and E. Bruck, J. Magn. Magn. Mater. **311**, 605 (2007).

[21] B. R. K. Nanda and I. Dasgupta, J. Phys.: Condens. Matter **15**, 7307 (2003).

[22] M. Zhang, X. Dai, H. Hu, G. Liu, Y. Cui, Z. Liu, J. Chen, J. Wang, and G. Wu, J. Phys.: Condens. Matter **15**, 7891 (2003).

[23] E. Sasioglu, L. M. Sandratskii, and P. Bruno, J. Appl. Phys. **98**, 063523 (2005).

[24] L. Offernes, P. Ravindran, and A. Kjekshus, J. Alloys Compd. **439**, 37 (2007).

[25] H. Luo, Z. Zhu, G. Liu, S. Xu, G. Wu, H Liu, J. Qu, and Y. Li, Physica B **403**, 200 (2008).

[26] I. Galanakis, K. Ozdogan, and E. Sasioglu, J. Appl. Phys. **104**, 083916 (2008).

[27] V. A. Dinh, K. Sato, and H. K. Yoshida, J. Phys. Soc. Jpn. **77**, 014705 (2008).

[28] V. A. Dinh, K. Sato, and H. K. Yoshida, IEEE Trans. Magn. **45**, 2663 (2009).

[29] V. A. Dinh, K. Sato, and H. K. Yoshida, J. Comput. Theor. Nanosci. **6**, 2589 (2009).

[30] M. P. Ghimire, Sandeep, T. P. Sinha, and R. K. Thapa, J. Alloys Compd. **509**, 9742 (2011).

[31] M. Singh, H. S. Saini, S. Kumar, and M. K. Kashyap, Comput. Mater. Sci. **53**, 431 (2012).

[32] Z. Yao, Y. S. Zhang, and K. L. Yao, Appl. Phys. Lett. **101**, 062402 (2012).

[33] Y. Wu, B Wu, Z. Wei, Z. Zhou, C. Zhao, Y. Xiong, S. Tou, S. Yang, B. Zhou, and Y. Shao, Intermetallics **53**, 26 (2014).

[34] L. Feng, E. K. Liu, W. X. Zhang, W. H. Wang, and G. H. Wu, J. Magn. Magn. Mater. **351**, 92 (2014).

[35] S. Y. Lin, X. B. Yang, and Y. J. Zhao, J. Magn. Magn. Mater. **350**, 119 (2014).

[36] E. L. Habbak, R. Shabara, S. H. Aly, and S. Yehia, Physica B: Condens. Matter **494**, 63 (2016).

[37] J. Ma, V. I. Hegde, K. Munira, Y. Xie, S. Keshavarz, D. T. Mildebrath, C. Wolverton, A. W. Ghosh, and W. H. Butler, Phys. Rev. B **95**, 024411 (2017), and references therein.

[38] T. Roy, D. Pandey, and A. Chakrabarti, Phys. Rev. B **93**, 184102 (2016), and references therein.

[39] T. Roy and A. Chakrabarti, J. Magn. Magn. Mater. **423**, 395 (2017).

[40] K. H. J. Buschow and D. B. de Mooij, J. Less-Common Met. **99**, 125 (1984).

[41] Y. Ma, S. Yang, Y. Zhou, C. Wang, and X. Liu, Intermetallics **18**, 2105 (2010).

[42] A. Szytula, A. T. Pedziwiatr, Z. Tomkowicz, and W. Bazela, J. Magn. Magn. Mater. **25**, 176 (1981).

[43] S. Niziol, A. Bombik, W. Baielal, A. Szytula, and D. Fruchart, J. Magn. Magn. Mater. **27**, 281 (1982).

[44] A. Szytula, W. Bazela, and S. Radenkovic, J. Magn. Magn. Mater. **38**, 99 (1983).

[45] H. Fjellvag and A. F. Andresen, J. Magn. Magn. Mater. **50**, 291 (1985).

[46] S. Kaprzyk and S. Niziol, J. Magn. Magn. Mater. **87**, 267 (1990).

[47] G. A. Landrum, R. Hoffmann, J. Evers, and H. Boysen, Inorg. Chem. **37**, 5754 (1998).

[48] J. Wirringa, R. Wartchow, and M. Binnewies, Z. Kristallogr. NCS **215**, 197 (2000).

[49] Y. Y. Zhao, F. X. Hu, L. F. Bao, J. Wang, H. Wu, Q. Z. Huang, R. R. Wu, Y. Liu, F. R. Shen, H. Kuang, M. Zhang, W. L. Zuo, X. Q. Zheng, J. R. Sun, and B. G. Shen, J. Am. Chem. Soc. **137**, 1746 (2015).

[50] R. Fruchart, A. Roger, and J. P. Senateur, J. Appl. Phys. **40**, 1250 (1969).

[51] M. A. Nylund, M. M. A. Roger, J. P. Senateur, and R. Fruchart, J. Solid State Chem. **4**, 115 (1972).

[52] M. R. Montreuil, B. Deyris, and A. Michel, Mater. Res. Bull. **7**, 813 (1972).

[53] V. Johnson, Mater. Res. Bull. **8**, 1067 (1973).

[54] S. Ohta, T. Kaneko, H. Yoshida, and T. Kanomata, J. Magn. Magn. Mater. **150**, 157 (1995).

[55] S. Ishida, T. Takiguchi, S. Fuji, and S. Asano, Physica B **217**, 87 (1996).

[56] T. Kanomata, H. Endo, H. Yamauchi, Y. Yamaguchi, H. Yoshida, T. Kaneko, H. Aruga Katori, and T. Goto, Physica B **237–238**, 517 (1997).

[57] A. Koumina, M. Bacmann, D. Fruchart, M. Mesnaoui, and P. Wolfers, M. J. Condensed Matter **5**, 117 (2004).

[58] H. M. V. Noort, D. B. de Mooij, and K. H. J. Buschow, Phys. Status Solidi A **86**, 655 (1984).
[59] V. Johnson, Inorg. Chem. **14**, 1117 (1975).
[60] K. H. J. Buschow, J. H. N. van Vucht, P. G. van Engen, D. B. de Mooij, and A. M. van der Kraan, Phys. Status Solidi A **75**, 617 (1983).
[61] G. Kresse and J. Furthmüller, Phys. Rev. B **54**, 11169 (1996).
[62] G. Kresse and D. Joubert, Phys. Rev. B **59**, 1758 (1999).
[63] The VASP 5.2 program package is fully integrated in the MedeA platform (Materials Design, Inc.) with a graphical user interface enabling the computation of the properties.
[64] P. E. Blochl, Phys. Rev. B **50**, 17953 (1994).
[65] J. P. Perdew, K. Burke, and M. Ernzerhof, Phys. Rev. Lett. **77**, 3865 (1996).
[66] See Supplemental Material at http://link.aps.org/supplemental/10.1103/PhysRevB.99.205136. See the Tables S1–S8 and Figs. S1–S6 for additional information. The calculated formation energy and the lattice parameters of Co*BC*, Ni*BC*, and Pt*BC* alloys in different crystal structures, such as half-Heusler cubic $C1_b$ type, orthorhombic Co_2P/NiTiSi type, as well as hexagonal Fe_2P type and Ni_2In type, are shown in Tables S1, S2, and S3, respectively. Table S4 shows the (x, z) parameters corresponding to the 4c Wyckofff positions of the *A*, *B*, and *C* atoms in Co*BC*, Ni*BC*, and Pt*BC* alloys, which are in the orthorhombic (*Pnma*) lowest energy structure. Furthermore, in Table S5, x parameters corresponding to the 3f and 3g Wyckofff positions of *A* and *B* atoms in Co*BC*, Ni*BC*, and Pt*BC* alloys which are in the hexagonal ($P\bar{6}2m$) lowest energy structure are shown. The total and partial spin magnetic moments and spin polarization of the stable Co*BC*, Ni*BC*, and Pt*BC* alloys in the cubic as well as in the noncubic lowest energy structures are tabulated in Tables S6, S7, and S8, respectively. Figure S1 shows the simulated XRD patterns of PtCrSn and NiMnAs alloys where the E_{form} is equal (PtCrSn) and somewhat close (NiMnAs) in two different structures. Figure S2 shows the hexagonal ($P6_3/mmc$) and orthorhombic (*Pnma*) structures of PtCrSn oriented in different planes, indicating an identical relative internal arrangement of atoms in the unit cell. Figure S3 shows the semicore and valence-band DOS of PtCrSn in hexagonal ($P6_3/mmc$) and orthorhombic (*Pnma*) structures. The flow chart in Fig. S4 shows the stability information of the 18 cubic compounds. Figures S5 and S6 show the total spin magnetic moments of the stable Co*BC*, Ni*BC*, and Pt*BC* alloys in noncubic orthorhombic as well as hexagonal lowest energy structures, respectively.
[67] P. Blaha, K. Schwartz, G. K. H. Madsen, D. Kvasnicka, and J. Luitz, *wien2k, An Augmented Plane Wave Plus Local Orbitals Program for Calculating Crystal Properties* (Technische Universität Wien, Wien, Austria, 2002).
[68] M. Baral, M. Chattopdhyay, R. Jangir, A. Chakrabarti, and T. Ganguli, J. Magn. Magn. Mater. **475**, 675 (2019).
[69] J. T. Wang, D. S. Wang, C. Chen, O. Nashima, T. Kanomata, H. Mizuseki, and Y. Kawazoe, Appl. Phys. Lett. **89**, 262504 (2006).
[70] Y. Okubo, S. Eto, Y. Mitsui, K. Koyama, and S. Fujii, AIP Adv. **8**, 101432 (2018).